Spectral diversity of rocks and soils in Mastcam observations along the Curiosity rover's traverse in Gale crater, Mars

Melissa S. Rice[1], Christina Seeger[1,2], Jim Bell[3], Fred Calef[4], Michael St. Clair[5], Alivia Eng[1], Abigail A. Fraeman[4], Cory Hughes[1,6], Briony Horgan[7], Samantha Jacob[3], Jeff Johnson[8], Hannah Kerner[9], Kjartan Kinch[10], Mark Lemmon[11], Chase Million[5], Mason Starr[1,12], Danika Wellington[13]

[1] Western Washington University.

[2] California Institute of Technology.

[3] Arizona State University

[4] Jet Propulsion Laboratory.

[5] Million Concepts.

[6] University of Arkansas.

[7] Purdue University.

[8] The Johns Hopkins University Applied Physics Laboratory.

[9] University of Maryland.

[10] Niels Bohr Institute, University of Copenhagen.

[11] Space Science Institute.

[12] Georgia Institute of Technology.

[13] KBR, Inc.

Corresponding author: Melissa Rice (melissa.rice@wwu.edu)

Key Points:

- The diversity in Mastcam multispectral data from sols 0-2302 is encapsulated by 9 rock spectral classes and 5 soil spectral classes.
- The major spectral differences in Mastcam spectra across Curiosity's traverse are attributable to hematite and other Fe-oxides.
- Comparisons of soil vs. rock spectra indicate that locally-derived sediments are not significantly contributing to the spectra of soils.

Abstract

The Mars Science Laboratory (MSL) Curiosity rover has explored over 400 meters of vertical stratigraphy within Gale crater to date. These fluvio-deltaic, lacustrine, and aeolian strata have been well-documented by Curiosity's in-situ and remote science instruments, including the Mast Camera (Mastcam) pair of multispectral imagers. Mastcam visible to near-infrared (VNIR) spectra can broadly distinguish between iron phases and oxidation states, and in combination with chemical data from other instruments, Mastcam spectra can help constrain mineralogy, depositional origin, and diagenesis. However, no traverse-scale analysis of Mastcam multispectral data has yet been performed. We compiled a database of Mastcam spectra from >600 multispectral observations and quantified spectral variations across Curiosity's traverse through Vera Rubin ridge (sols 0-2302). From principal component analysis and an examination of spectral parameters, we identified 9 rock spectral classes and 5 soil spectral classes. Rock classes are dominated by spectral differences attributed to hematite and other oxides (due to variations in grain size, composition, and abundance) and are mostly confined to specific stratigraphic members. Soil classes fall along a mixing line between soil spectra dominated by fine-grained Fe-oxides and those dominated by olivine-bearing sands. By comparing trends in soil vs. rock spectra, we find that locally derived sediments are not significantly contributing to the spectra of soils. Rather, varying contributions of dark, mafic sands from the active Bagnold Dune field is the primary spectral characteristic of soils. These spectral classes and their trends with stratigraphy provide a basis for comparison in Curiosity's ongoing exploration of Gale crater.

Plain Language Summary

The Curiosity rover's Mastcam instrument is a pair of cameras that take images in visible and near-infrared wavelengths. Mastcam spectra can distinguish between different types of iron-bearing minerals. During Curiosity's traverse through a variety of sedimentary rock types in Gale crater, Mars, the rover has acquired more than 600 Mastcam multispectral observations, but no previous studies have analyzed the full dataset. In this study, we compiled a database of Mastcam spectra from the first 2302 sols (Martian days) of Curisoity's mission and analyzed spectral trends across the traverse. We define 9 classes of spectra for rocks and 5 classes of spectra for soils, and we observe that different classes occur in different locations. The major spectral differences are due to the mineral hematite and other iron oxides. By comparing the trends in rock spectra to nearby soils across the traverse, we find that the soils are not made of the same minerals as the local rocks, but are dominated by sands from the active Bagnold Dune field. These spectral classes and their trends will be a basis of comparison for Curiosity's ongoing exploration of Gale crater.

1 Introduction

The Mars Science Laboratory (MSL) Curiosity rover has traversed more than 26 km and gained over 400 m in elevation since landing in Gale crater in 2012. Across this traverse, Curiosity has encountered a wide variety of sedimentary units within the crater floor and Aeolis Mons (informally called Mt. Sharp), which have been divided into stratigraphic formations within three major groups: the Bradbury Group (Grotzinger et al., 2015; Rice et al., 2017), the Siccar Point Group (Fraeman et al., 2016; Banham et al., 2018), and the Mt. Sharp Group (Stack et al., 2019; Edgar et al., 2020). The chemical and mineralogical compositions of these units have been studied in detail using remote sensing observations from the Chemistry and Camera (ChemCam) Laser Induced Breakdown Spectroscopy (LIBS) instrument, subsurface observations from the Dynamic Albedo of Neutrons (DAN) instrument, *in-situ* observations from the Alpha Particle X-Ray Spectrometer (APXS), and laboratory measurements from the Sample Analysis at Mars (SAM) and Chemistry and Mineralogy (CheMin) investigations. In addition to these quantitative composition techniques, Curiosity's Mast Camera (Mastcam) multispectral instrument can help to constrain mineralogy and extend the mapping of compositional units beyond where other instrument measurements have been acquired.

Mastcam is unique among Curiosity's scientific payload in that it can quickly acquire spectral information over broad spatial areas. At distances of a few meters, Mastcam multispectral images can document spectral diversity across a given outcrop in combination with textural information such as grain size, sedimentary structures, diagenetic features, and contact geometries. At distances of up to several kilometers, Mastcam observations correlated with the larger-scale stratigraphy can enhance mineralogical and stratigraphic maps made from orbiter data, such as from the Mars Reconnaissance Orbiter (MRO) Compact Reconnaissance Imaging Spectrometer for Mars (CRISM) and High Resolution Imaging Science Experiment (HiRISE) instruments.

Each Mastcam camera is mounted ~1.9 m above the Martian surface on the rover's mast and utilizes an 8-position filter wheel in front of a 1600 x 1200 pixel Bayer-patterned charge-coupled device (CCD) (Malin et al., 2017). When images are acquired through multiple filter positions with both cameras at the same pointing, each pixel in the resulting multispectral observation includes visible to near-infrared (VNIR) reflectance data at up to 12 unique wavelengths, including the Bayer red, green and blue (RGB) broadbands. Mastcam's filter set has direct heritage from the Imager for Mars Pathfinder (IMP) (Smith et al., 1997; Bell et al., 2000), the Mars Exploration Rover (MER) Panoramic Camera (Pancam) instruments (Bell et al., 2003; 2006), and Phoenix's Surface Stereo Imager (SSI) (Smith et al., 2008). However, Mastcam multispectral analyses are inherently different from those of previous imagers because of two complicating factors: the addition of the Bayer filters on the CCD (which each set of narrowband wavelengths must "see through") and the different focal lengths of the two cameras (34 mm for Mastcam left and 100 mm for Mastcam right, which produce significantly different fields of view).

On their own, Mastcam spectra do not provide unique mineral identifications, but they can broadly distinguish between different iron mineralogies and oxidation states. In combination with chemical data from Curiosity's other instruments, Mastcam spectra can help constrain mineralogy, depositional origin, and diagenesis. In observations from the first part of Curiosity's traverse, through the fluvio-deltaic sequences within the Bradbury Group (Vasavada, 2014) and the fluviolacustrine mudstones and siltstones of lower Murray Formation of the Mt. Sharp Group (Grotzinger et al., 2015), Mastcam spectra of soils and rock targets are largely consistent with basaltic materials with variable coatings of nanophase ferric oxide from airfall dust (Wellington et al., 2017). Outcrop targets where the Dust Removal Tool (DRT) and/or drill were used, however, show more spectral diversity (Wellington et al., 2017). Mastcam spectra of bright, fracture-filling veins within the Bradbury Group, in combination with measurements of elevated Ca and S by ChemCam and APXS (e.g., Nachon et al., 2014; Wrapin et al., 2016), are consistent with hydrated Ca-sulfate phases in some occurrences (Vaniman et al., 2014). At locations where high-Mn concentrations have been observed by ChemCam LIBS, such as in the Kimberley formation (Rice et al., 2017), Mastcam spectra are very dark and flat, consistent with Mn-oxides

(Lanza et al., 2016). Rocks identified as meteorites exhibit distinct spectral profiles characterized by both relatively low overall reflectance as well as positive spectral slope throughout the Mastcam wavelength range (Wellington et al., 2018; 2019)

Further along Curiosity's traverse through the Murray formation, Mastcam spectra of specific outcrops near Marias Pass, where DAN measurements predicted high-SiO_2/low-FeO bedrock, are consistent with opaline silica, leading to their interpretation as a silicic volcaniclastic layer (Czarnecki et al., 2020). Observations of active aeolian sand deposits at the Bagnold Dunes are consistent with the mafic compositions observed from obit by CRISM (Lapotre et al., 2017) with variable contributions of Fe-oxide-bearing sands (Johnson et al., 2017; 2018). At the Sutton Island outcrops, Mastcam spectral variations have been attributed to Fe/Mg-smectites in lacustrine mudstones with variable iron mobilization during diagenesis (Haber et al., 2020). Near and atop the Vera Rubin ridge, outcrops have shown even more variability in their Mastcam spectral properties, which are consistent with varying contributions coarse-grained gray hematite vs. nanophase and fine-grained red crystalline hematite, interpreted as variable diagenesis by oxidizing fluids (Fraeman et al., 2020a; Horgan et al., 2020; Jacob et al., 2020).

The Mastcam multispectral analyses summarized above have all focused on isolated geographic regions along Curiosity's traverse and/or specific types of surface features. No studies to date have synthesized Mastcam multispectral observations for the entire dataset across the traverse. However, understanding how outcrop properties vary with lithology and elevation throughout the full stratigraphy is key to interpreting the depositional history of Gale crater and the complex history of diagenesis. Indeed, such systematic analyses of chemical variations with stratigraphy (chemostratigraphy), as derived from by ChemCam (e.g., Frydenvang et al., 2020) and APXS (e.g., Thompson et al., 2020) data, have been critical to contextualizing individual outcrops within the larger geologic history of fluviolacustrine activity, diagenetic alteration, and subsequent erosion in Gale crater. Thus, this work is motivated by the need for a comprehensive analysis of the full Mastcam multispectral dataset. Our objectives are to identify the predominant Mastcam spectral classes encountered to date, to analyze their distributions across Curiosity's traverse, and to correlate the observed spectral variations with trends in the stratigraphy.

To this end, we analyzed the full suite of Mastcam multispectral images and compiled a comprehensive multispectral database from surface observations up to sol 2302 (through Curiosity's exploration of Vera Rubin ridge). In the following sections, we describe the first systematic analysis of Mastcam spectra from all regions, rock types, and soils across the rover's extended traverse. This comprehensive approach allows us to develop "best practices" for analyzing Mastcam multispectral observations and to establish conventions for working with the dataset, taking into account the complicating presence of Bayer filters and separate fixed focal lengths. We generate "spectro-stratigraphic" columns that document spectral variations across the traverse by plotting spectral parameters vs. elevation, which we qualitatively compare to changes in lithology and quantitatively compare to laboratory measurements of mineral spectra. We also leverage principal component analysis (PCA) to identify the major components of spectral variability in the database, which we use to identify the major rock and soil spectral classes that Curiosity has encountered to date. Ultimately, we synthesize these observations to present a holistic view of the Mastcam spectral diversity in Gale crater.

2 Methods

2.1 Mastcam Filter Set

The Mastcam instrument is a pair of cameras referred to as M34 (left camera) and M100 (right camera). Each camera obtains images through a Bayer pattern of broadband RGB filters and telecentric microlenses bonded onto the charge-coupled device (CCD) (Malin et al., 2017). The cameras' eight-position filter wheels enable the collection of spectra in 12 unique wavelength bands centered between 445 and 1013 nm (Table 1; Figure 1) (Bell et al., 2017). Each filter wheel includes a broadband filter with a near-infrared cutoff for Bayer RGB images, six narrowband geology filters (three of which are nearly identical in the left and right cameras for stereo imaging), and a solar filter for atmospheric monitoring (e.g., tau measurements) and certain astronomical observations (solar transits of Phobos and Deimos).

Table 1. *Mastcam RGB Bayer and geology filters effective center wavelengths (λ_{eff}) and half-widths at half-maximum (HWHM), after Bell et al. (2017).*

Mastcam Left (M34)		Mastcam Right (M100)	
Filter Position	**λ_{eff} ± HWHM (nm)**	**Filter Position**	**λ_{eff} ± HWHM (nm)**
L0 (Red Bayer)	640 ± 44	R0 (Red Bayer)	638 ± 44
L0 (Green Bayer)	554 ± 38	R0 (Green Bayer)	551 ± 39
L0 (Blue Bayer)*	481 ± 37	R0 (Blue Bayer)*	483 ± 37
L1	527 ± 7	R1	527 ± 7
L2	445 ± 10	R2	447 ± 10
L3	751 ± 10	R3	805 ± 10
L4	676 ± 10	R5	937 ± 11
L5	867 ± 10	R4	908 ± 11
L6	1012 ± 21	R6	1013 ± 21

** The blue Bayer band center wavelengths differ from those reported by (Bell et al., 2017), see text for details.*

We have adopted 481 and 483 nm as the center wavelength of the blue Bayer filter for the left and right eye, respectively (Table 1), as opposed to the 493 and 495 nm used by Bell et al. (2017). This follows from the pre-flight radiometric calibration of Mastcam-Z on the Mars-2020 mission Perseverance rover (Hayes et al., 2021). Because Mastcam and Mastcam-Z use the same Bayer and infrared cut-off filters (L0/R0), and have the same ON Semiconductor (formerly

Kodak) KAI-2020CM CCD, the two instruments should have the same effective wavelengths for all three Bayer channels. Hayes et al. (2021) show that the band centers of the Bayer green and red channels are nearly the same for Mastcam and Mastcam-Z, as expected, but the blue channels for Mastcam-Z match the vendor's prediction of 480 nm (and not the reported Mastcam values).

Independently, we used Mastcam multispectral data from Mars to estimate the Bayer effective band centers. We compared two sets of atmospheric multispectral images: a deeply orange sky during the peak of the July 2018 global dust storm (sol 2086, mcam11116) and a faintly bluish Sun (sol 2100, mcam11211). Spectra from both the Sun and the dusty sky should have very smooth profiles across the wavelength range of the Bayer filters (e.g., Lemmon et al., 2019). By taking a ratio of the dust storm sky to the Sun radiances, we produced a spectrum in which any misidentified filter should stand out. This sky/Sun ratio (Figure S1) eliminates instrumental response and photometric variations caused by different angles for the right and left cameras. By assuming the narrowband filter positions are well known, we fitted the Bayer positions to a smooth spectral profile and found 481.1 nm and 482.7 nm for the Bayer blue left and right camera wavelengths, respectively. Further analyses using dusty sky observations from sols 1629 and 2105 also yielded the same results for the revised Bayer band center wavelengths.

Hayes et al. (2021) also suggest that the "saw tooth" pattern observed near 652 nm in the Mastcam spectral profiles (see Figure 3 in Bell et al. (2017)) may be related to a grating transition and not Mastcam's actual spectral response. This feature has the strongest influence on the broadband Bayer red profile. Therefore, for our convolutions of laboratory spectra to Mastcam bandpasses (Section 2.7), we used the Bayer red transmission profile as measured for Mastcam-Z, in addition to the Bayer blue profile of Hayes et al. (2021), in combination with the profiles for the other Mastcam filters as reported by Bell et al. (2017) (Figure 1).

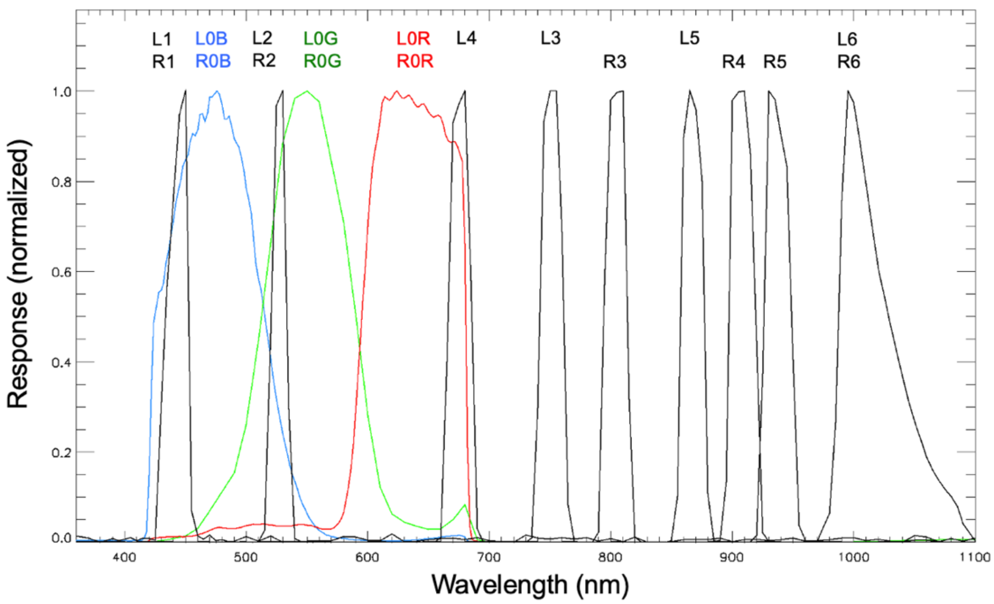

Figure 1. *Transmission profiles of Mastcam filters used for convolutions of laboratory spectra. Profiles are as reported by Bell et al. (2017), with the exception of the Bayer blue and Bayer red filters, which have been updated based on the radiometric calibration of Mastcam-Z, which uses the same infrared cutoff filters and CCD detectors as Mastcam (Hayes et al., 2021).*

2.2 Mastcam Image Calibration

We calibrated Mastcam observations to radiance using pre-flight calibration coefficients from radiance products available via the NASA Planetary Data System (PDS) (Bell et al., 2017). We converted radiance to radiance factor (*I/F*, or "IOF," where *I* is equal to the measured scene radiance and πF is the solar irradiance received at the surface at the time of the observation) using associated observations of the Mastcam calibration target. To correct for the effects of airfall dust on the calibration target, we used two-stream radiative transfer models (Kinch et al., 2015). We converted radiance factor to relative reflectance (R^*) (Reid et al., 1999), also known as the "reflectance factor" (Hapke et al., 1993), by:

$$R^* = \mathrm{IOF} / \cos(i) \qquad (1)$$

where i is the solar incidence angle (provided in the observation metadata, see Section 2.4). This procedure was first developed from the MER Pancam calibration pipeline (Bell et al., 2006). Absolute calibration accuracy for Mastcam's filter set is 10-15% or better (Bell et al., 2017).

Images calibrated to R^* are partially "atmospherically corrected" because observations of the Mastcam calibration target also include near-simultaneous measurements of the Mastcam sky illumination component of the scene radiance (Kinch et al., 2015; Bell et al., 2017). However, the calibration of Mastcam images to R^* assumes that all illumination comes from a point source at the position of the Sun, and that the scene is perfectly flat and parallel to the calibration target (and therefore the solar incidence angle remains constant within an image). To minimize uncertainties that arise from these assumptions, the Curiosity team typically acquires Mastcam multispectral observations as close to local noon as possible; routine exceptions are photometry observations, which are intentionally acquired at multiple times of sol to document the same surface under multiple illumination geometries (e.g., Johnson et al., 2013).

2.3 Compilation of a Mastcam Multispectral Database

Curiosity has acquired Mastcam multispectral observations within all major stratigraphic units (Table 2) and across most elevation intervals over the traverse (Figure 2b). We compiled a comprehensive database of Mastcam spectra that sample the diversity observed across Curiosity's traverse, including a total of 624 observations as described below. This tally excludes 38 multispectral observations acquired between sols 0-2302 because of extensive shadowing, failed image execution, incomplete downlink, and/or complicated mosaic acquisition (which pose challenges to our multispectral analysis tools and have been deferred to future analyses) (Table S3).

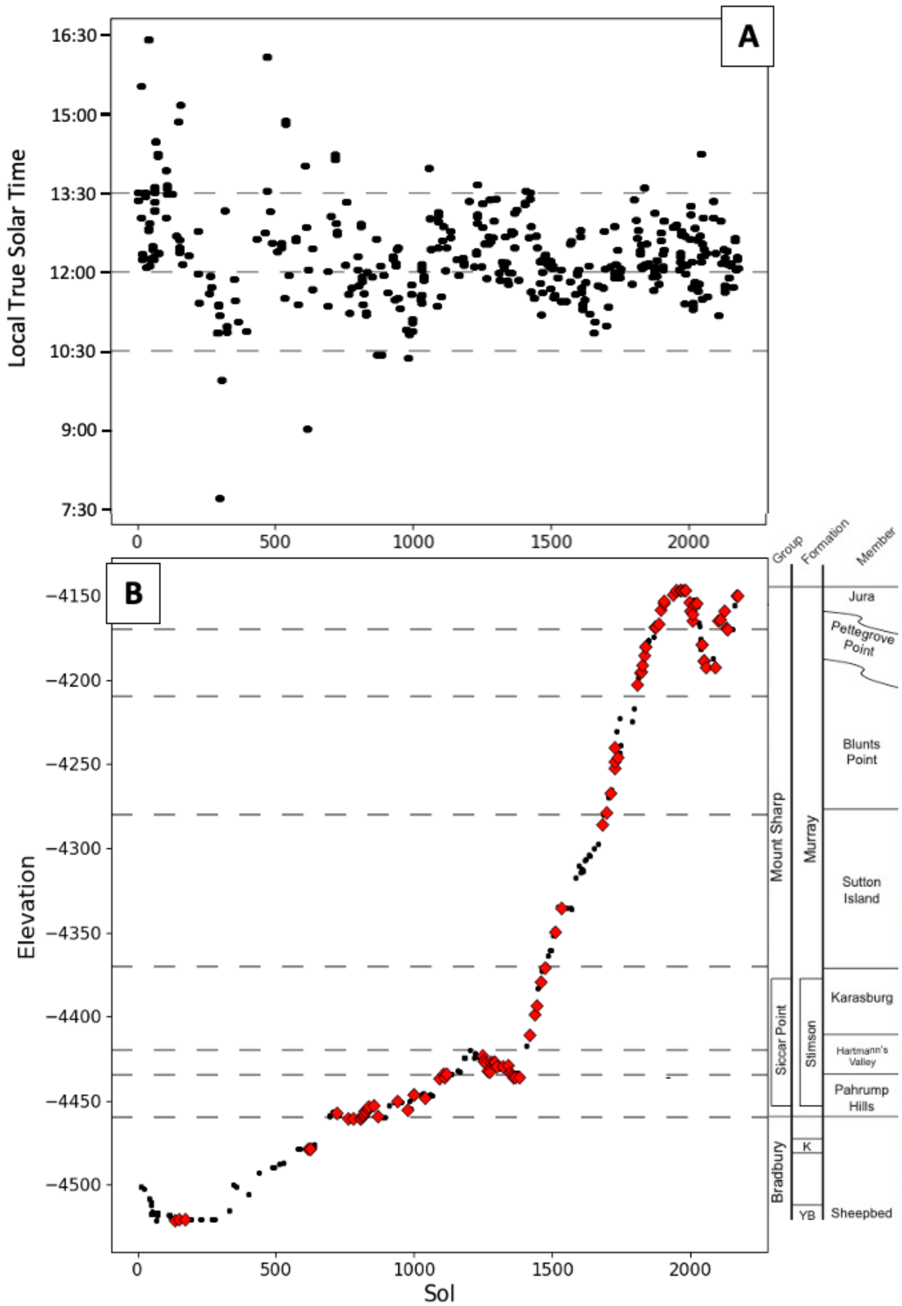

Figure 2. *Frequency of Mastcam multispectral images acquired along Curiosity's traverse: (a) Time of day (Local True Solar Time) for all multispectral surface observations (excluding photometry sequences). Assumptions in the calibration pipeline do not apply at low Sun angles, so we generally restrict our analyses to observations acquired 10:30-13:30 LTST (range indicated by horizontal dashed lines); (b) Rover elevation vs. sol for each multispectral surface observation (details provided in Table 2). Red points indicate the locations of low-dust targets (including those brushed by the Dust Removal Tool (DRT), broken rocks and drill fines). Approximate elevation intervals of stratigraphic members (Table 2) are marked by dashed horizonal lines.*

Table 2. *Summary of Mastcam multispectral observations of rocks acquired through the stratigraphy of Bradbury Rise and Mt. Sharp up to sol 2302. Some dedicated soil observations include no rocks in the field of view and are not listed here; some observations tallied here include rocks from multiple members. Descriptions of stratigraphic units can be found in Grotzinger et al. (2015); Rice et al. (2017); Stack et al. (2019); and Edgar et al. (2020).*

Group	Formation	Member	Elevation Range (m)	Sol Range	Number Mastcam Observations
Mt. Sharp	Murray	Jura	-4174.7 – -4139.9	1866-1302	61
		Pettegrove Point	-4200.1 – -4155.4	1812-2153	62
		Blunts Point	-4280.5 – -4180.6	1688-1807	26
		Sutton Island	-4371.2 – -4286.2	1475-1682	44
		Karasburg	-4410.8 – -4360.8	1417-1492	26
		Hartmann's Valley	-4435.6 – -4410.4	1355-1405	22
		Pahrump Hills	-4461.3 – -4419.9	758-1276	86
Siccar Point	Stimson		-4450.4 – -4379.5	943-1462	77
Bradbury	The Kimberley	Beagle*	-4479.2	620	1
		Dillinger*	-4479.2 – -4456.7	614-626	4
		Liga*	-4479.2 – -4478.7	582-620	10
		Square Top*	-4478.7	581-582	2
	Yellowknife Bay	Sheepbed*	-4521.0 – -4520.3	133-298	36
		Gillespie *	-4520.5 – -4518.2	116-301	11
		Glenelg*	-4519.3 – -4516.6	53-323	38
	(Unclassified)		-4520.5 – -4456.7	13-728	66

** Not shown on the stratigraphic column in Figure 2.*

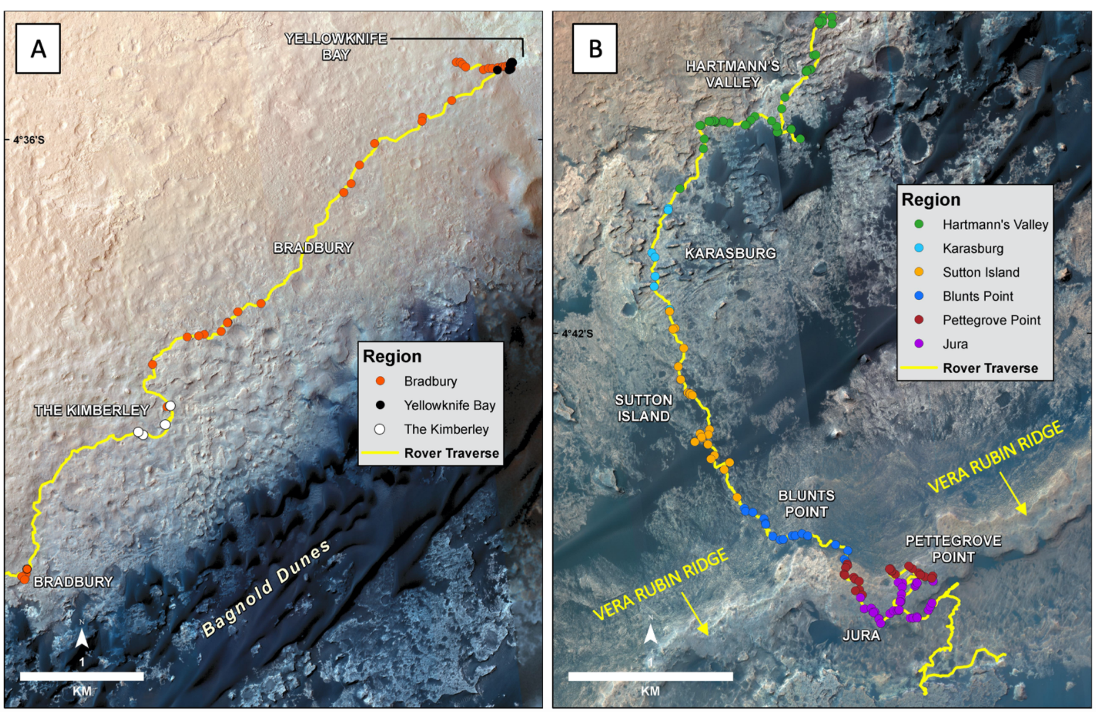

Figure 3. *Maps of Curiosity's traverse and locations of Mastcam multispectral observations for (a) sols 0-750 in the Bradbury Group, and (b) sols 750-2302 in the Mt. Sharp Group, with observations within the Murray formation labeled (Siccar Point Group targets occur throughout this sol range, see Table 2).*

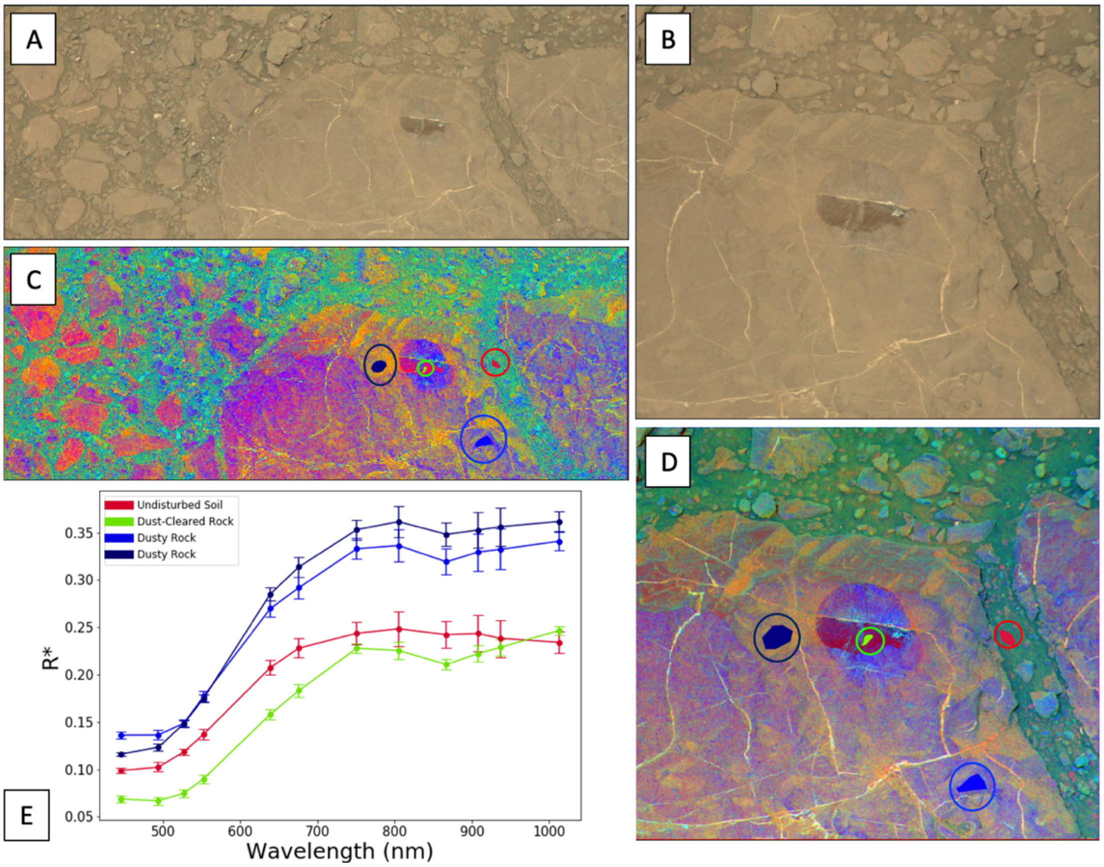

Figure 4. *Example of region of interest (ROI) selection of color endmembers in a full-filter Mastcam multispectral observation of the Hex River DRT spot (sol 1885, mcam09853): Bayer red, green and blue (RGB) composites from the (a) L0 image and (b) R0 image; Decorrelation stretch (DCS) images, with ROI positions overlain, made with filters (c) L1, L2 and L6, and (d) R1, R2 and R6; (e) Spectra extracted from ROIs (with left- and right-eye spectra scaled to 1012 nm and stereo filters averaged). The DRT spot size is ~4.5 cm in diameter.*

For each Mastcam multispectral observation, we characterized the spectral variability in the scene by manually identifying color end members through a visual inspection of the approximate true color (ATC) images, false color images and decorrelation stretch (DCS) products (Gillespie et al., 1986) (e.g., Figure 4). We produced false color and DCS composites from combinations of Mastcam filter images that produced the largest color contrasts for each observation. While the specific filter combination that produces the most variability in false color and DCS images is not necessarily the same for each scene, we found that R1/R2/R6 and L1/L2/L6 produced the best color contrast in most observations. We identified end members as groupings of pixels that exhibit distinct colors in the false color and DCS products and also represent geologically-distinct surfaces (as identified in the ATC images). We took care to identify color end members corresponding to different geologic materials, and to distinguish these from color variations that may result from small differences in local viewing geometry (e.g., the multiple facets of a homogenous rock). In instances of variable dust cover on an otherwise homogenous surface, we selected end members on both the most- and least-dusty regions. We generally excluded regions where color end-members were present only in the M34 images but not in the M100 images, such as the magenta/orange hues seen in the left of Figure 4c, except for targets of particular geologic interest (e.g, candidate meteorites) or significance to the mission (e.g., drill tailings).

We extracted a representative spectrum of each end member by manually selecting pixels from regions of interest (ROIs) in the right and left camera images separately. All spectra are included in Table S2. In selecting ROIs, we adhered to a system of "best practices" to ensure the extraction of geologically meaningful spectra with minimal noise:

1. We used a minimum ROI size of 30 unsaturated pixels in the M34 images, with rare exceptions for very small features (e.g, narrow veins).
2. We generally collected spectra from contiguous regions, but occasionally selected ROIs from non-contiguous regions of the same spectral endmember (as could be identified in DCS images) to increase the total pixel count.
3. Where possible, we extracted spectra from near-horizontal surfaces near the center of the image to best match the assumptions made in the Mastcam calibration pipeline (Bell et al., 2017).
4. We avoided edges of geologic features to mitigate the effects of small (pixel-scale) shifts

between filter images that may be present due to de-Bayering and/or chromatic aberration.

5. We avoided surfaces exhibiting specular reflections, shadows, and/or rover hardware.

Multiple people (2-4) inspected each observation to verify that the selected ROIs corresponded to end members within the scene and consistently followed the best practices procedures. Locations of ROIs are documented in Supplementary Data Set S1. (shown overlain on DCS images for each multispectral observation).

We flagged pixels with 11-bit data number (DN) values greater than 2000 in raw images as "saturated" and excluded them from ROI averages on a per-filter basis. In the spectra shown, we represent "error bars" in $R*$ as the standard deviation among the selected ROI pixels; this is a measure of the homogeneity of the pixel values within the ROI, and is generally much larger than the instrumental error (Bell et al., 2017).

2.4 Compilation of Relevant Metadata

Each endmember spectrum was compiled with relevant metadata. Observation-level and ROI-specific metadata are included with the spectral database (Table S2). A number of the metadata fields specific to each observation were taken directly from the Mastcam images' Planetary Data System version 3 (PDS3) headers, including: the Mastcam sequence identifier (seq ID); target name; day of the mission (sol); time of day measured as the local true solar time (LTST) at the start of the observation; camera focal distance; site index and rover drive number (which resets after each site index increment, so that site index and drive number together give a unique rover position). We also included metadata for the season in the form of solar longitude (L_s), which is the Mars-Sun angle measured from the Northern Hemisphere spring equinox.

Atmospheric optical depth was also included for each observation, given as τ (“tau”) (Lemmon et al., 2019; Guzewich et al., 2019); interpolated values were used for times when direct measurements were not available.

Geographic information was taken from localization data provided for each rover position in the PDS, including: latitude, longitude, total traverse distance (odometry), and rover elevation. Depending on the observation geometry, the elevation of the targets in the scene may be significantly different from the rover’s elevation; however, most multispectral observations are of workspace targets that are close to the same elevation as the rover (<1 m difference), and more distant targets are identified by the camera focal distance in the PDS3 image headers. When making spectro-stratigraphic plots of parameters vs. elevation, we exclude distant targets with large uncertainties in their elevations.

Observation geometries were calculated using instrument data in the PDS3 headers: the incidence angle (*i*) was calculated from the site frame SOLAR_ELEVATION field minus 90 degrees, and the emission angle (*e*) was taken as the INSTRUMENT_ELEVATION plus 90 degrees. The phase angle (*g*) is defined as the angle between the incidence and emission vectors, which is given by:

$$cos\, g = cos\, i\, cos\, e + sin\, i\, sin\, e\, cos(\Delta\phi) \quad (2)$$

where $\Delta\phi$ is the angle between the projection of the incidence vector ϕ_i and emission vector ϕ_e on the surface, given as the difference between the two absolute azimuths, or $\Delta\phi = |\phi_i - \phi_e|$ (e.g., Shepherd et al., 2008). The incidence vector is taken directly from the SOLAR_AZIMUTH header value in the PDS3 images, and the emission vector is the INSTRUMENT_AZIMUTH value plus 180 degrees. For our metadata, we recorded the geometries for the center of the image at the start of the observation (from the headers of the first filter acquired, usually L0).

Table 3. *Feature types and subtypes assigned to each Mastcam spectrum and total number of spectra from each type in our database.*

Feature Type			Description	Number of Spectra
Soils		Undisturbed Soil	Sand and/or soil that has not been disturbed by the rover	637
		Disturbed Soil	Sand and/or soil that has clearly been disrupted by the rover's wheels, scoop, and/or drilling activities	128
Rocks	Drill Fines	Drill Tailings	The annulus of fine-grained material surrounding the hole after drilling	41
		Dump Piles	Drill core material that was crushed and sieved and dumped on the ground following a drill campaign	33
	Dust-Cleared Targets	DRT Target	Rock surfaces that have been brushed by the Dust Removal Tool (and are relatively dust-free)	119
		Broken Rock	Freshly-exposed interior surfaces of rocks that have been broken open by Curiosity's wheels and/or drill activities	31
	Dusty Targets	Dusty Rock	Undisturbed rock surfaces that do not include a high density of concretions and/or nodules	1509
		Vein	Light-toned fracture-fill material	82

Each spectrum was assigned one of the geologic "feature types" listed in Table 3. We classified all rock spectra in our multispectral database as either "in-place" or "float" (not attached to outcrop). Float rocks can either be eroded components of bedrock or allochthonous material (e.g., impact ejecta or meteorites). Rocks that were not clearly distinguishable as float rocks or in-place outcrop (e.g., partially-buried rocks) were classified as "in-place." In observations with both in-place and float rocks with the same textural and color properties, we preferentially extracted spectra from the in-place rock.

We assigned specific lithology information (group, formation, and member) from the stratigraphic column of Edgar et al. (2020) (Table 2). Using the multispectral database and these metadata, we examined how key spectral parameters vary with stratigraphy and other aspects of geology and geography. In the spectro-stratigraphic plots and parameter space analyses presented here, we restrict our analyses to observations acquired between 10:30 and 13:30 LTST (local noon ± 1.5 hours), as some assumptions in the calibration pipeline break down at lower Sun angles. Figure 2a shows the starting LTST of Mastcam multispectral observations in our database (excluding photometry sequences); only a small subset of observations falls outside this range, mostly from early in the mission.

2.5 Quantification of Spectral Parameters

To study variations in Mastcam spectra, we quantified a variety of spectral parameters specific to the Mastcam filter set (Table 4). Band depths were calculated using the definition from Clark & Roush (1984):

$$D = 1 - \frac{R_b}{R_c} \tag{2}$$

where R_b is the reflectance at the band center λ_b and R_c is the reflectance of the continuum at the same wavelength as R_b, defined as a straight line passing through two "shoulder" positions on either side of the absorption feature. For left and right shoulder reflectance values R_L and R_R at wavelength positions λ_L and λ_R, the reflectance of the continuum is:

$$R_c = xR_L + yR_R \tag{3}$$

where

$$x = \frac{\lambda_R - \lambda_b}{\lambda_R - \lambda_L} \tag{4}$$

and

$$y = 1 - x \tag{5}$$

To characterize broad spectral profiles (e.g., from unresolved bands at the short- or long-wavelength ends of the Mastcam spectrum), previous multispectral analyses have used slope and ratio parameters interchangeably (e.g., Farrand et al., 2008). Here, we explored slope vs. ratio parameters for the same Mastcam bands to establish a convention for characterizing spectral shape. Slope is calculated using the difference of reflectance values divided by the difference in wavelengths, which means the overall brightness is a factor in the equation. Ratio, however, is independent of the overall albedo, and will be the same in IOF or *R** spectra. Therefore, ratio is not sensitive to inherent uncertainties in the *R** correction (Equation 1), which assumes that incidence angle is the same for all pixels in the field of view and for all filters in the observation. For example, spectra with the same "red ratio" value (751 nm / 442 nm) can have a wide range of "red slope" values (442 nm to 751 nm), depending upon their overall reflectance values at 751 nm (Figure 2). We want to minimize the influence of uncertainties in absolute reflectance to best explore spectral shapes to characterize spectral diversity and interpret mineralogy; we therefore use ratio parameters exclusively (Table 4).

Table 4. *Summary of spectral parameters used to characterize Mastcam spectra.*

Camera	Parameter	Formula	Possible Mineralogic Indicators
Left	L6 (1012 nm) / L3 (751 nm) ratio	R^*_{1012} / R^*_{751}	Used as a proxy for NIR profile; values < 1.0 are consistent olivine, clinopyroxene, and basaltic glasses; values >1.05 can be indicative of iron meteorites
Left	L1 (527 nm) band depth	$1 - R^*_{527} / (0.23R^*_{447} + 0.77R^*_{551})$	Larger value can indicate higher degree of Fe oxidation (e.g., Farrand et al., 2008)
Left	L3 (751 nm) / L2 (445 nm) ratio	R^*_{751} / R^*_{445}	Termed "red/blue ratio" and can indicate "redness" of spectra; larger values are consistent with higher degrees of oxidation
Left	L3 (751 nm) / L1 (527 nm) ratio	R^*_{751} / R^*_{527}	A modified version of the "red/blue ratio"; values >1.1 are consistent with iron meteorites (e.g. Wellington, 2018)
Left	L3 (751 nm) / L4 (676 nm) ratio	R^*_{751} / R^*_{676}	Indicates the location of the reflectance maximum between 600-800 nm; values > 1.0 have peak positions closer to 751 nm, consistent with ferric phases; values <1.0 have peak positions closer to 676 nm, more consistent with ferrous phases
Left	L5 (867 nm) band depth	$1- R^*_{867}/(0.556R^*_{751}+0.444R^*_{1012})$	Largest values are consistent with presence of fine-grained, red crystalline hematite, and smaller positive values consistent with other Fe-oxides. Negative values indicate a convex NIR profile more consistent with olivine, pyroxenes and nontronite (e.g. Horgan et al., 2020)
Right	805 / 937 nm ratio	R^*_{805} / R^*_{937}	Large positive values may indicate broad Fe absorptions in the NIR; values close to 1.0 indicate "flat" NIR profiles and are consistent with phases that are spectrally neutral in the NIR (e.g., pure sulfates). Small values are consistent with hematite.
Right	937 / 1013 nm ratio	R^*_{937} / R^*_{1013}	Used to quantify the spectral "downturn" or "uptick" in the longest Mastcam wavelength. Values > 1.0 with otherwise flat NIR profiles are consistent with a hydration band at ~980nm (Rice et al., 2010). Large values paired with large 805/937nm ratios are consistent with broader 900-1000nm absorptions (e.g., olivines, pyroxenes). Values < 1.0 are more consistent with 800-900nm absorptions (e.g., hematite).

2.6 Scaling Spectra from the Two Cameras

The different spatial resolutions of the two Mastcam cameras (M34 and M100) introduce complications to the analysis of the multispectral dataset. Full spectra can only be acquired from the area of overlap between the two eyes, and the number of pixels in ROIs covering the same spatial extent differs greatly. The left (M34) bands have lower spatial resolution and therefore fewer pixels to sample and less total signal. We find that the left (M34) filter values are often lower than the right filter values (Figure S3), but we have not observed any correlations between any of our metadata parameters (e.g., sol, LTST, ROI size, or viewing geometry) and the ratios of reflectance between equivalent bands in the left and right cameras. The disparity between the two cameras is most easily explained by differences in their FOVs and ROI sizes, as the left filter ROIs are more susceptible to pixel-scale image mis-registrations and other noise.

The offset in absolute reflectance requires that we carefully consider strategies for combined analysis of spectra from the two cameras. We can join spectra from the two cameras by normalizing the left- and right-eye spectra to their average R^* value at a single overlapping band position (L1/R1, L2/R2, L0B/R0B, L0G/R0G, R0R/R0R or L6/R6; Table 1) and then averaging the R^* values of the other stereo positions. The effects of scaling spectra to these different positions can have implications for interpreting the mineralogy. Many spectra are not impacted by the choice of scaling (those with left/right band ratios close to 1.0; Figure S3). However, for other spectra, the near-infrared shape can vary significantly depending upon which overlapping band position is used to scale the two cameras. For example, in spectra of hematite-bearing DRT targets scaled to L6 (1012 nm) / R6 (1013 nm) (Figure 5), the L5 (867 nm) band shape matches the broad absorption profile of laboratory hematite spectra. But when spectra of some hematite-bearing targets are scaled to other wavelength positions, a jagged “sawtooth” pattern is induced in their NIR profiles, with the L5 (867 nm) band as an apparent peak above the adjacent R3 (805 nm) and R5 (937 nm) values (e.g., the Fort Brown DRT target; Figure 5). For other hematite-bearing targets, when the left- and right-Mastcam spectra offsets are smaller, a “sawtooth” pattern is not introduced but the L5 (867 nm) band shape narrows when scaled to filters other than L6 (1012 nm) / R6 (1013 nm) (e.g., the Hexriver DRT target; Figure 5).

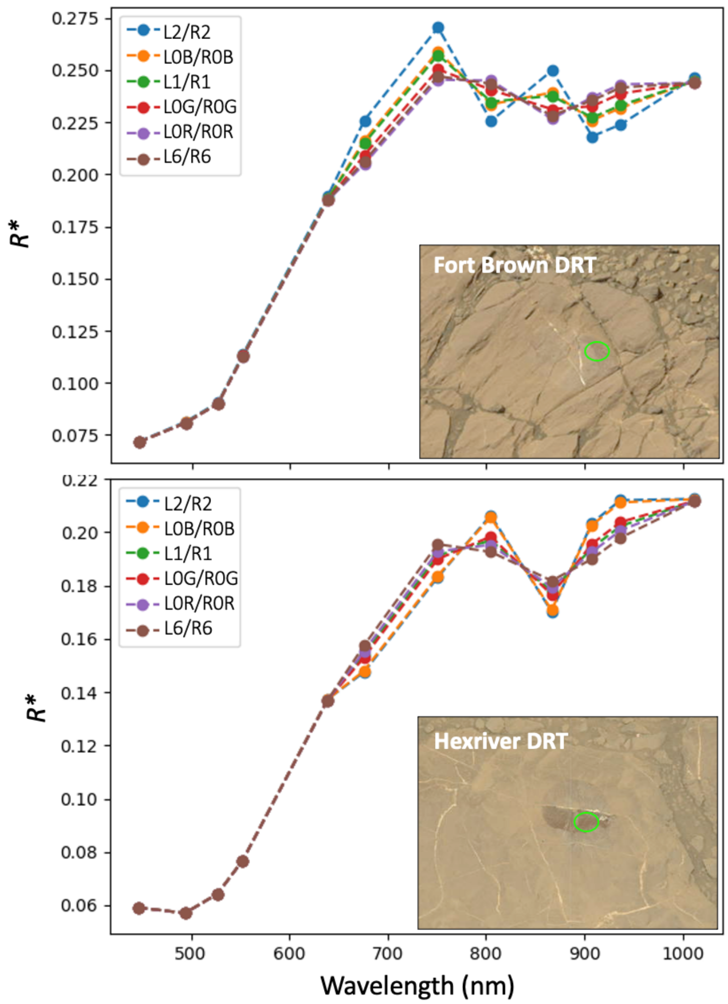

Figure 5. *Examples of how scaling Mastcam spectra to different overlapping left- and right-camera filter positions can influence spectral shape. In both examples, the same data from a hematite-bearing target within the Jura formation are shown as six spectra, each scaled to a different set of overlapping filters. Above: Spectra from the Fort Brown DRT target (shown in the inset from sol 1876, mcam09813). Below: Spectra from the Hexriver DRT target (shown in the inset from sol 1885, mcam09853). Spectra were averaged from pixels within in the green circle; error bars are omitted for clarity. For scale, the dust-cleared DRT spots are ~4.5 cm in diameter.*

Therefore, when displaying full-filter spectra in this work, we always scale spectra in both cameras to the average at L6 (1012 nm) and R6 (1013 nm); this convention best reproduces the expected band profiles in Mastcam spectra targets of known mineralogy. We use caution when evaluating the shape of full spectra where the filters alternate between the two Mastcams (751-908 nm), especially when "sawtooth" patterns are present in the scaled spectra. In quantitative analyses, we also use filters exclusively from the left- or right-Mastcam when calculating band parameters (Table 4), obviating the effects of absolute reflectance offsets.

2.7 Comparisons to Laboratory Spectra

We performed an analysis of laboratory spectra as a baseline for comparison to and interpretation of Mastcam spectra. We convolved high-resolution laboratory spectra of these minerals to the Mastcam spectral bands with the algorithm described by Rice et al. (2010). For the stereo overlap positions, only the right Mastcam filter transmission profiles were convolved. A representative subset of minerals with prominent Fe^{2+} and/or Fe^{3+} absorptions was used for a Mastcam band parameter analysis (Figure 6), following Horgan et al. (2020), with additional meteorite spectra from Cloutis et al. (2010).

The spectral region covered by Mastcam's geology filters is particularly sensitive to iron-bearing primary basaltic minerals (e.g., Adams, 1974), secondary iron oxide and oxyhydroxide minerals (e.g., Singer, 1982; Morris et al., 1985); ferric sulfates, ferric carbonates, and iron-bearing clays (e.g., Sherman et al., 1982). The VNIR spectral properties of ferrous iron (Fe^{2+}) and ferric iron (Fe^{3+}) in various minerals have been extensively documented (e.g., Clark et al., 1990), and key spectral parameters can help distinguish between iron oxidation states, which we have adapted to the Mastcam filter set (Table 4). The L1 (527 nm) band depth parameter quantifies the depth of an absorption near 530 nm which, together with the L3 (751 nm) / L2 (445 nm) ratio (indicating a steep "red" profile from ~440-700 nm) can characterize relative amounts of Fe-oxides.

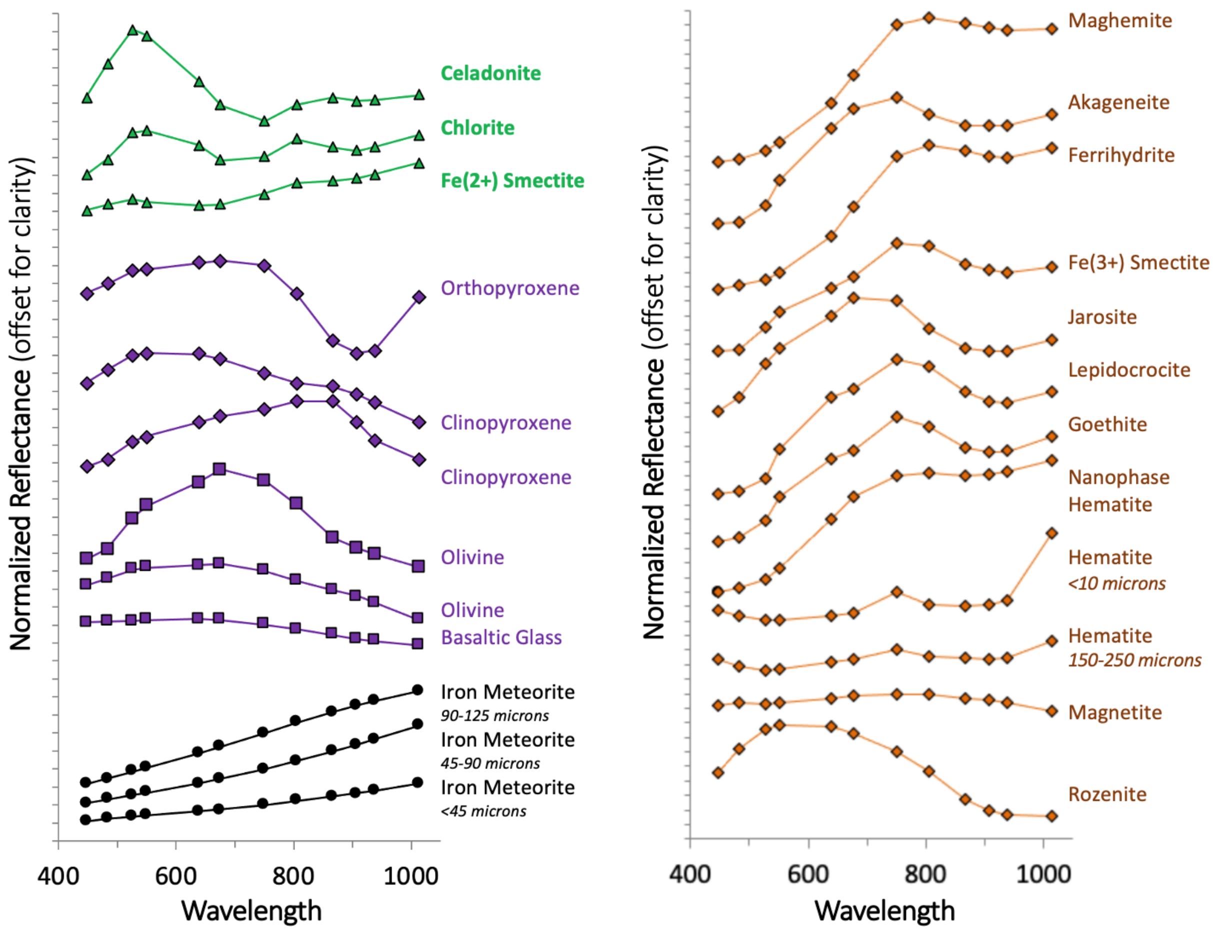

Figure 6. *Laboratory spectra of common primary and secondary Fe-bearing minerals and iron oxides, modified from Figure 3 of Horgan et al. (2020): ferrous alteration phases (green triangles); pyroxenes (purple diamonds); olivines and basaltic glass (purple squares); and ferric alteration phases (orange diamonds). Iron meteorite spectra (of Odessa at varying grain sizes) shown are from Cloutis et al. (2010) (black circles). Spectra have been convolved to Mastcam spectral bandpasses (Table 1), normalized to 1.0 at 751 nm, and offset for clarity.*

A broad spectral "hump" near 600 nm is consistent with ferrous phases, while most ferric phases have local maxima closer to 750 nm (Figure 6); these distinctions can be quantified as L3 (751 nm) / L4 (676 nm) ratios less than or greater than 1.0, respectively (Table 4). L3 (751 nm) / L4 (676 nm) ratios < 1.0 together with broad absorptions centered near 1000 nm (quantified as

L6 (1012 nm) / L3 (751 nm) ratios <1.0) are consistent with olivine, clinopyroxene or basalt glass (Figure 6). Ferric minerals typically have L6 (1012 nm) / L3 (751 nm) ratios >1.0, indicative of broad absorptions between 800 nm and 900 nm. Red, fine-grained hematite spectra exhibit particularly large L6 (1012 nm) / L3 (751 nm) ratios and strong bands centered at 867 nm; other ferric phases, in addition to orthopyroxene, exhibit deep absorption bands centered at 908 nm.

We also analyzed a representative suite of hydrated minerals, including borates, carbonates, chlorides, halides, hydroxides, perchlorates, phyllosilicates, other hydrated silicates, ices, sulfates and zeolites (Kokaly et al., 2017; Cloutis et al., 2006; Crowley, 1991; Rice et al., 2013). From this survey of library spectra, we identified 49 minerals with H_2O and/or OH absorptions in Mastcam's wavelength range, which have generally narrow absorption bands centered from 949-1020 nm (Table S1). Example spectra of minerals with a range of band centers, depths and widths are shown in Figure 7. Generally, the depth of the band correlates with the amount of hydration (e.g., Rice et al., 2010). However, not all hydrated and/or hydroxylated minerals exhibit related absorption features that are resolvable in this wavelength range; for example, this weak overtone feature is easily masked by more prominent absorptions centered between 900-1000 nm in many iron-bearing minerals, such as nontronite (see Fe^{3+} smectite in Figure 6).

In the Mastcam-convolved spectra, the depth of the narrow hydration absorption at R6 (1013 nm) is strongly dependent on the band center and width of the feature (Figure S4). Mastcam is only able to detect this band at a threshold of >1% for minerals with absorptions centered longward of ~980 nm (e.g., epsomite, bischofite, ulexite and gypsum; Figure 7). The position of the H_2O and/or OH feature in the majority of hydrated and hydroxylated minerals, however, is centered between ~950-980 nm. For minerals with narrow bands centered in this range, the hydration is invisible to Mastcam (e.g., analcime, brucite; Figure 7). Therefore, the depth of the R6 (1013 nm) feature in Mastcam spectra (Table S1) does not necessarily correlate with amount of H_2O and/or OH; while the presence of the band can indicate the presence of hydrated minerals, the absence of an R6 (1013 nm) band does *not* indicate an absence of hydration. Also, for absorptions centered closer to 950 nm, such as in saponite (Figure 7) and other phyllosilicates (Figure S4), the band may be detectable by Mastcam's R5 (937 nm) filter.

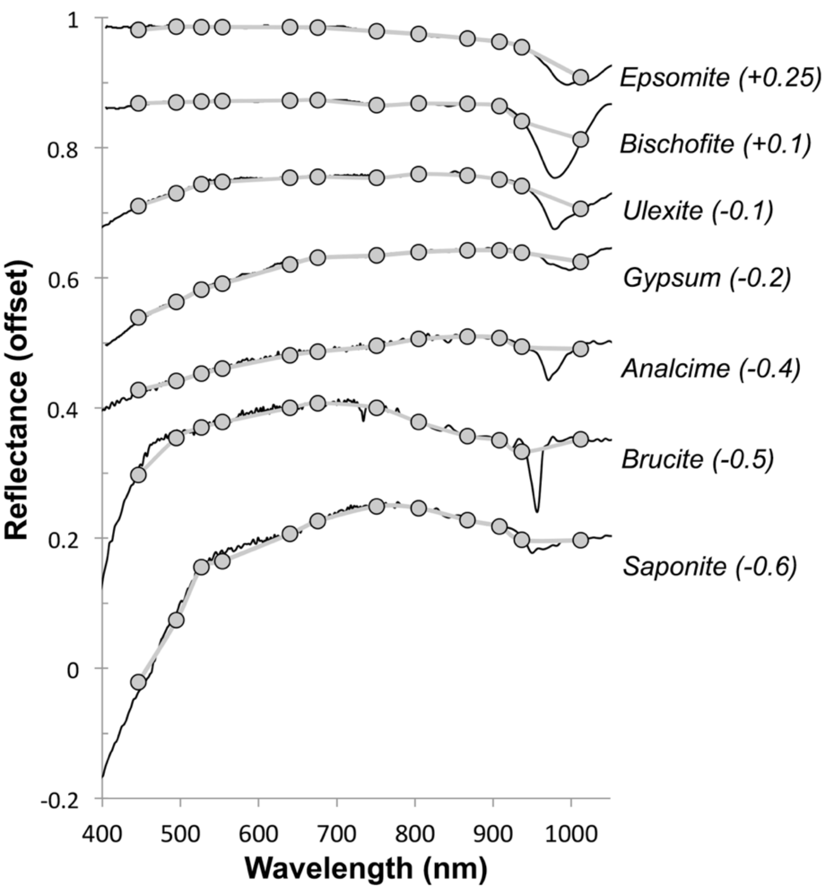

Figure 7. *Examples of hydrated mineral spectra from existing libraries plotted over the Mastcam wavelength range (black lines), with reflectance values convolved to Mastcam bandpasses (gray points). All spectra are offset for clarity (offset values shown next to mineral names). Epsomite, bischofite, ulexite and gypsum are examples of minerals with Mastcam "R6 hydration band" depths ≥ 1.0%. Analcime, brucite and saponite are examples of minerals with hydration bands that are not detectable by Mastcam's R6 filter. Spectral libraries are listed in Table S1.*

Spectral parameters that characterize minerals with >980 nm hydration absorptions are the R5 (937 nm) / R6 (1013 nm) ratio and the R3 (805 nm) / R5 (937 nm) ratio (Table 4), which quantify the absorption at R6 (1013 nm) and the broad NIR profile (which is flat or slightly positively-sloping in most hydrated minerals). Distinguishing between the hydrated phases that exhibit these characteristics is not possible using Mastcam spectra alone. However, in combination with chemistry data from other Curiosity instruments (such as elevated Ca and S in fracture-filling veins, as indicated by ChemCam and APXS), the presence of these spectral features in Mastcam spectra can help refine mineralogic interpretations (e.g., gypsum vs. anhydrite or bassanite for calcium sulfates).

2.8 Spectral Classification

We visually inspected Mastcam spectra for VNIR features associated with iron-bearing mineralogy and/or hydration, and quantified key parameters for all spectra as shown in Table 4. In order to maximize the variance within the Mastcam spectral dataset, we also used principal component analysis (PCA), a dimensional reduction technique in which a linear orthogonal transformation transforms a dataset into a new coordinate space (e.g., Davis, 1973). We represented the data as a linear sum of orthogonal principal components, which were chosen in the PCA process to be in order of decreasing variance. We normalized spectra to 1.0 at their peak reflectance prior to performing the PCA so that the components would represent variance in spectral shape independent of overall albedo. To exclude noisy spectra from the analysis (which may result from ROIs with very few pixels, image misregistration, or accidental inclusion of shadowed regions), we filtered the dataset by the size of their average error bars, excluding spectra with average pixel standard deviation greater than 0.02 reflectance units.

We used the Scikit-learn Python package (https://scikit-learn.org/stable/about.html; Pedregosa et al., 2011) to perform PCA on two subsets of the Mastcam multispectral database: rocks and soils (Table 3). We plotted the contributions of the various PCs to each spectrum against one another to represent Mastcam spectra in component space, where unique spectral endmembers were identified by their separation from the rest of the data cloud. We examined the shapes of the spectra with the largest and smallest values of each PC to infer the specific spectral features that contribute to the components. This general approach was previously applied to identify spectral classes from Pancam datasets along the Spirit and Opportunity rover traverses (e.g., Farrand et al., 2006; 2008; 2013).

We defined spectral classes by synthesizing PCA results (Section 3.4) with spectro-stratigraphic plots and visual inspections of spectra across the traverse (Sections 3.1-3.2). We identified these classes based on similar spectral characteristics that are compositionally meaningful and which are less likely to result from calibration uncertainties, overall brightness of the scene, and/or effects of scaling the two Mastcam spectra (as discussed in Section 2.7). To that end, we avoided defining classes based on albedo alone, or based on the relative reflectance values of adjacent filters between the two Mastcams (e.g., the L5 (867 nm) vs. R4 (908 nm) values). We do not define classes based on any single outlier spectrum; in order to be defined as a class, we require that the same spectral features be observed in multiple Mastcam observations.

3 Results

3.1 Rock Spectral Variability

3.1.1 Trends with Stratigraphy and Dust Cover

Where Curiosity's DRT had been employed, we extracted spectra from the resulting dust-cleared rock surface, as well as spectra from adjacent, dusty rock surfaces (e.g., Figure 8). Direct comparisons of dusty and dust-cleared targets demonstrate that dust consistently masks rock spectra, resulting in higher reflectance (especially at longer wavelengths), muted absorption features, and smaller L3/L2 (751 nm/445 nm) ratios. Across the entire dataset, dust-cleared rocks tend to exhibit greater L5 (867 nm) band depths than dusty rocks, particularly on Vera Rubin ridge. They also exhibit consistently lower L3/L2 (751 nm/445 nm) ratios, especially in the lower Murray formation where L1 (527 nm) band depths are also shallower for dust-cleared rocks.

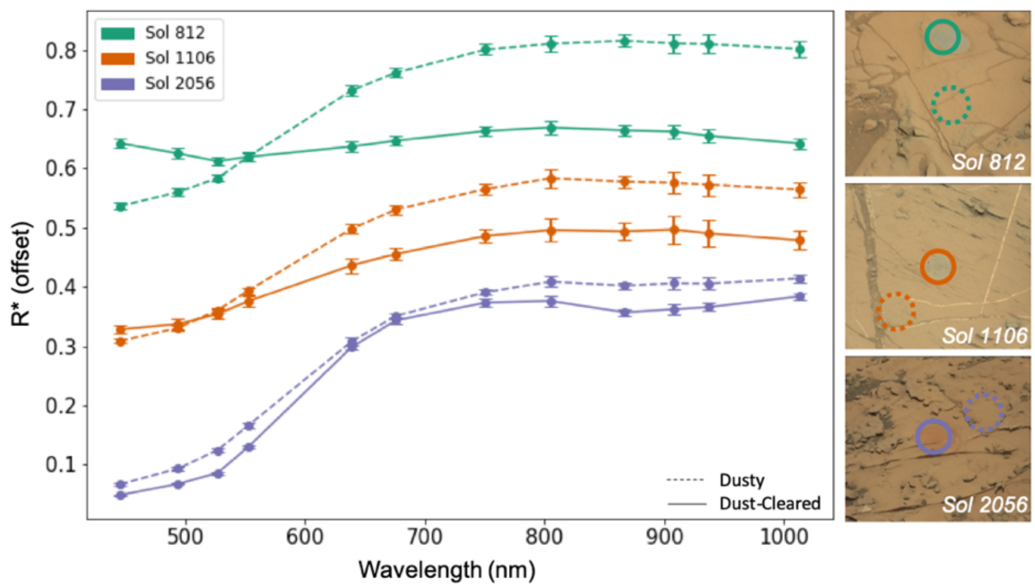

Figure 8. *Spectral variability of example dusty and dust-cleared targets. Dust consistently masks the rock spectra. (left) Mastcam spectra, where solid lines indicate dust-cleared rock targets, and dashed lines indicated adjacent dusty bedrock. Spectra are averaged within each ROI, offset for clarity, and shown with one standard deviation error bars. (right) Mastcam RGB images of three example observations with spectra extracted from ROIs within DRT spots (solid circle) and adjacent dusty bedrock (dashed circle). Targets are Mojave (Pahrump Hills member; sol 812, mcam03564), Winnipeg (Stimson formation; sol 1106, mcam 04915), and Duluth (Blunts Point member; sol 2056, mcam10897). DRT spots are ~40mm in diameter.*

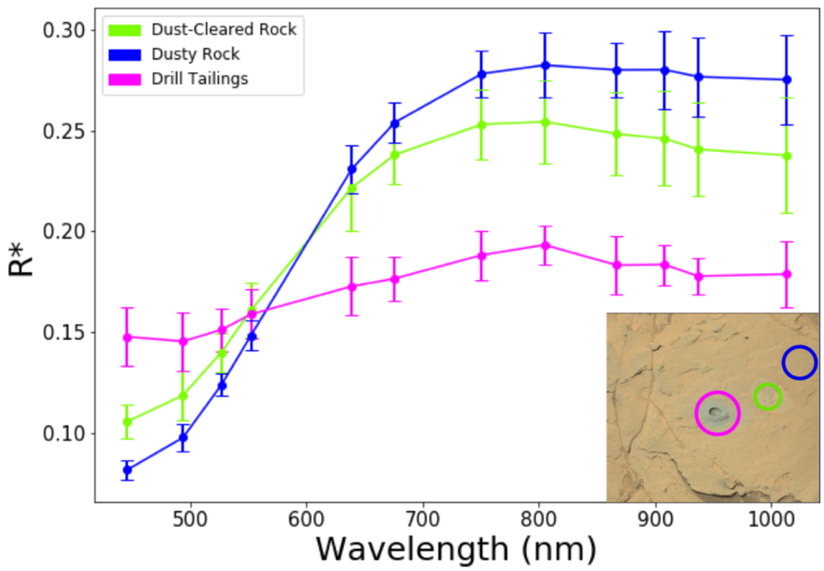

Figure 9. *Example Mastcam spectra extracted from adjacent dusty rock (blue), dust-cleared rock (green), and drill tailings (magenta). Inset Mastcam RGB image indicates ROI locations in Big Sky mini drill hole observation (sol 1118, mcam04983; for scale, drill hole is ~16 mm in diameter. Spectra are averaged within each ROI and shown with one sigma error bars.*

Like dust-cleared sections of rock, drill targets can provide even more insight into the rocks' spectral properties; drill tailings (Table 3), while varying in grain size (generally >5µm in diameter; Rampe et al., 2020), are largely dust-free and offer a bulk rock sample from depths of a few cm. Although the middle interval of the Murray formation has sparse drill samples due to time needed to develop new drilling techniques after the drill feed mechanism failure, every stratigraphic member (Edgar et al., 2020) was still sampled. Spectra from drill fines present similar advantages as DRT spots for investigating rock spectral properties, and they have little to no dust cover, although they are texturally different than intact rock surfaces. For example, in the Big Sky observation on sol 1118, we extracted spectra from drill tailings, an adjacent DRT spot, and typical dusty bedrock surface (Figure 9). The drill tailings spectrum is much flatter than the others, with a lower L3/L2 (751 nm/445 nm) ratio and generally deeper absorption features than the dustier counterparts, particularly in the NIR.

In the traverse through the Bradbury Group and into the lower Murray formation (below the Sutton Island member), spectra from drill fines are consistent with corresponding DRT spectra in L5 (867 nm) band depth but tend to have lower L3/L2 (751 nm/445 nm) ratios and shallower L2 (527 nm) absorption features (Figure 10). In these strata, we observe a clear progression of decreasing redness (lower L3/L2 (751 nm/445 nm) ratios) from dusty rock surfaces to DRT targets to drill fines at the same elevations. However, these relationships are more complicated within and stratigraphically above the Sutton Island member, where some drill fines are redder than adjacent DRT targets, with deeper L2 (527 nm) absorptions. These trends have been attributed to the presence of hematite in the Murray formation, which is redder at fine grain sizes than in outcrop (Horgan et al., 2020; Jacob et al., 2020).

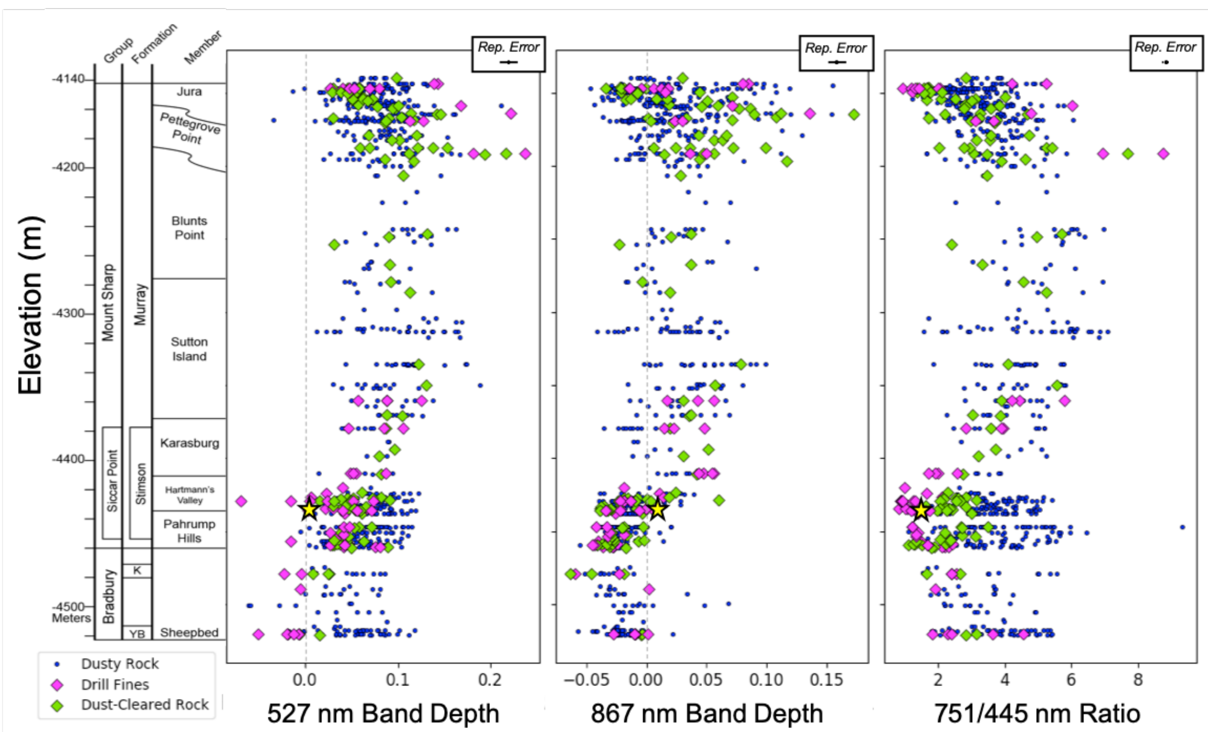

__Figure 10.__ Spectral variability for all dusty and dust cleared rocks, with the addition of all drill tailings and dump piles (together referred to as drill fines). Example target Big Sky drill tailing values are indicated by yellow stars (spectra shown in Figure 14).

Overall, drill fines are more spectrally diverse in their L3/L2 (751 nm/445 nm) ratios than dust-cleared and dusty targets. Juxtaposing spectra from these three feature types demonstrates the degrees to which dust masks the spectra and highlights which spectral features are most useful in the dusty rock spectrum to reflect the actual spectral signature of the underlying rock. Specifically, the L5 (867 nm) band depth is the most consistent across all target types (Figure 10), indicating that this band is the least influenced by surface dust. Indeed, laboratory studies have shown that thin covers of dust simulants have stronger masking effects on VIS than NIR spectral features (e.g., Johnson & Grundy, 2001).

3.1.2 Float vs. In-Place Rock Spectra

It is rare to encounter large, cohesive bedrock outcrops in Gale crater; rather, most of Curiosity's traverse has been across an expansive, broken pavement. Our multispectral database includes 1102 in-place rock spectra and 556 float rock spectra. Float rocks are distributed throughout the stratigraphic sequence but are comparatively sparse in the Blunts Point member (Figure 11). In general, float rocks are spectrally consistent with proximal in-place targets, as would be expected for rock fragments weathering out of local outcrop. Only float rocks found in the Sutton Island and Jura members are spectrally distinct from their in-place counterparts at equivalent elevations (Figure 11), interpretations for which are given in Section 4.

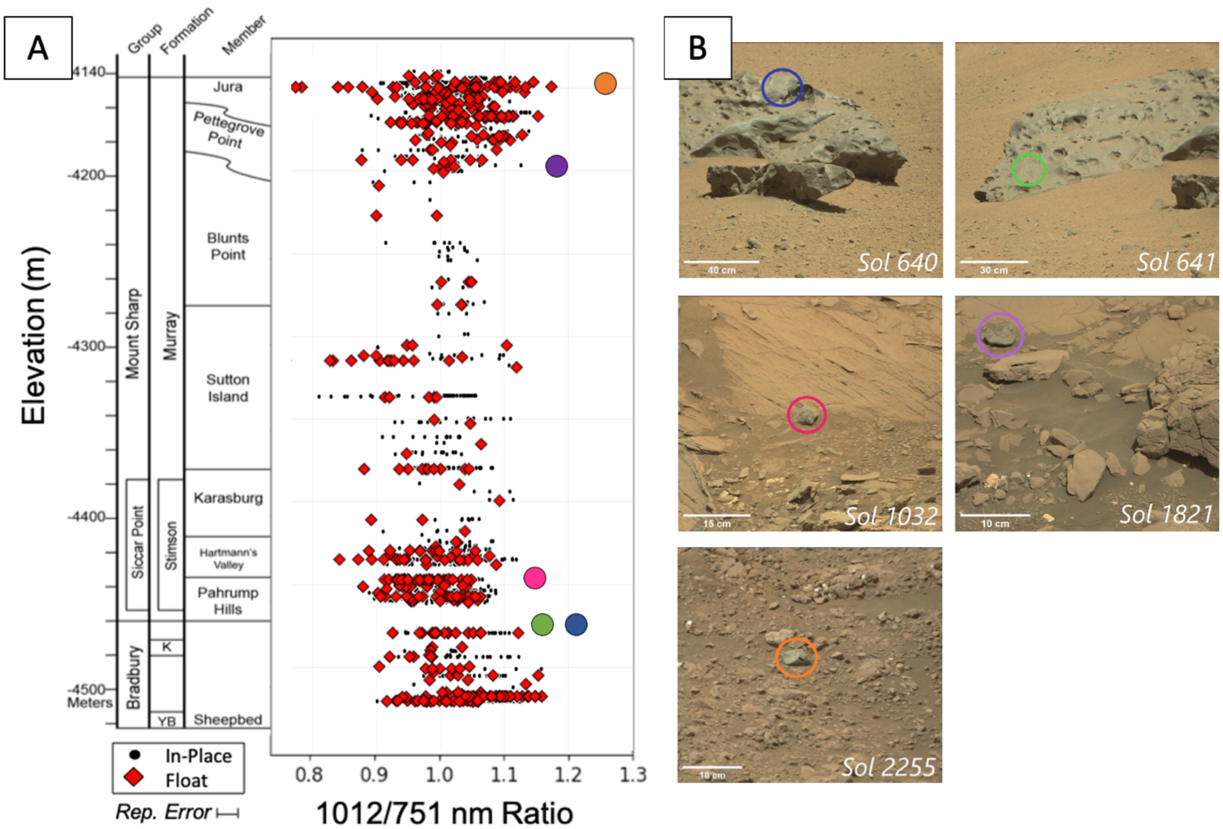

Figure 11. *Float rock and in-place rock spectra across the traverse: (a) 1012 nm / 751 nm ratio for float rocks (red diamonds) compared to in-place rocks (black points). Spectra from five outliers (large circles) are shown in Figure 17. (b) Mastcam R0 images of float rocks with anomalously high 1012 nm / 751 nm ratios from the following observations: Lebanon (sols 640 and 641), Cottonwood (sol 1032), Mustards Island (sol 1821), and Newburgh (sol 2255). ROIs of spectra shown in Figure 12 are within the circled areas.*

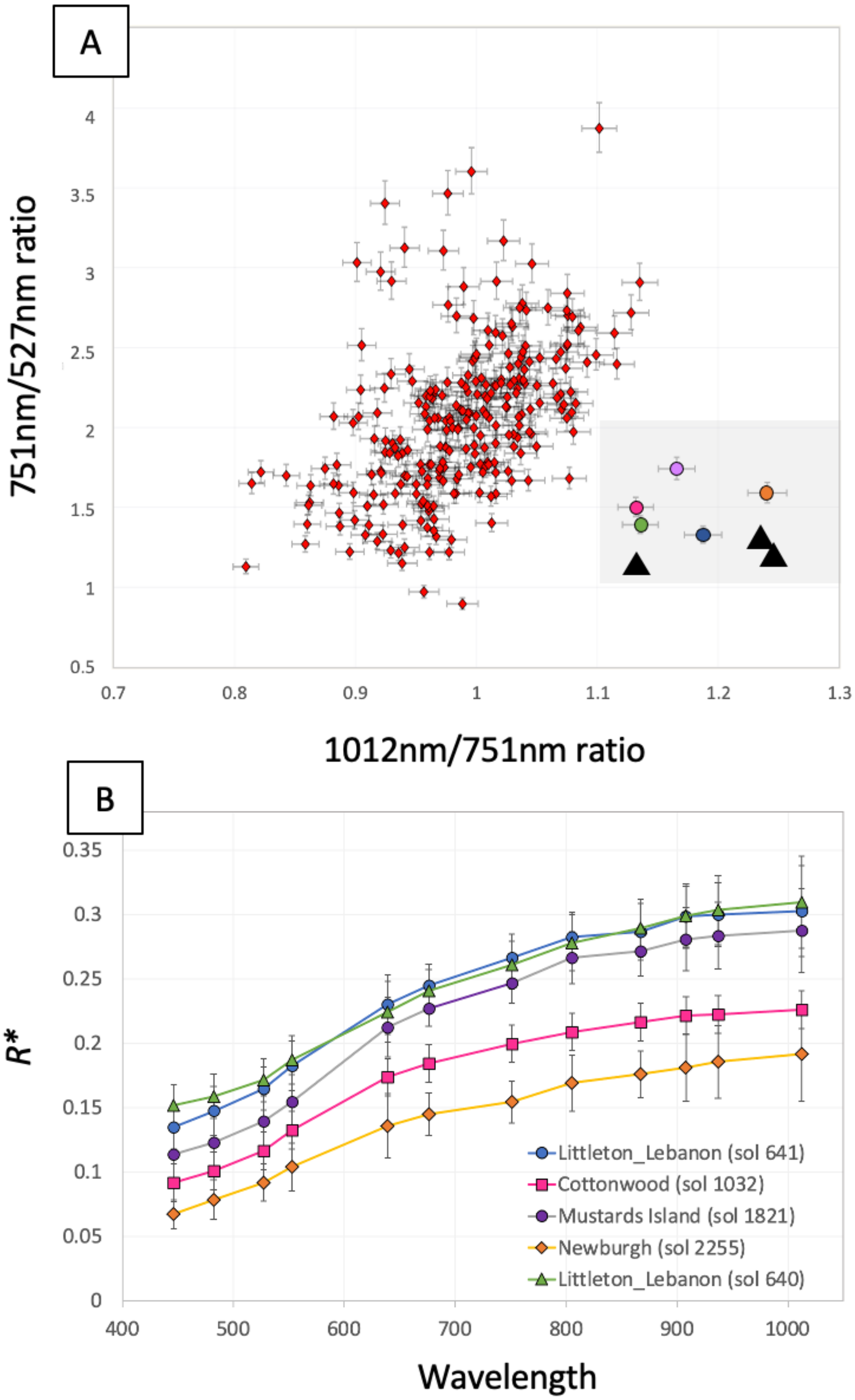

Figure 12. *Identification of iron meteorites in Mastcam float rock spectra. (a) Parameters that distinguish candidate meteorites (colored circles) from the rest of the float rock dataset (red diamonds), with values for lab spectra of iron meteorites shown as black triangles (full lab spectra shown in Figure 6).(b) Mastcam spectra of the five iron meteorite candidates shown in the gray region in (a), images of which are shown in Figure 11.*

Several anomalous float rocks were noted in previous studies as being candidate meteorites or meteorite fragments (based on morphology, chemistry and/or spectral properties). Those that have been confirmed as meteorites with chemical measurements have dark grayish colors and distinct positive NIR slopes in Mastcam spectra (Wellington, 2018). These spectral properties can be quantified with low L3/L2 (751 nm/527 nm) ratios and high L6/L3 (1012 nm/751 nm) ratios, respectively. In the parameter space shown in Figure 12, candidate meteorites plot in the lower right corner, separately from all other rock targets. The five points with L6/L3 (1012 nm/751 nm) ratios greater than 1.1 include float rock spectra from: Lebanon (sols 640 mcam02729; sol 641 mcam02718), Cottonwood (sol 1032, mcam04511), Mustards Island (sol 1821, mcam09401), and Newburgh (sol 2255, mcam12069). Each of these has previously been reported as a candidate meteorite (Wellington et al., 2018; 2019; Johnson et al., 2020); therefore, we do not identify any new meteorite candidates in our multispectral database but confirm the utility of these parameters for searching for meteorites along Curiosity's ongoing traverse.

3.1.3 Fracture-Filling Veins

We searched the multispectral database for hydration absorptions at R6 (1013 nm), as have been associated with Ca-sulfate veins at Meridiani Planum (Squyres et al., 2012; Farrand et al., 2013) and with opaline silica at Gusev crater (Wang et al., 2008; Rice et al., 2010; Ruff et al., 2011), and found no features that are clear indicators of hydration in vein or other rock spectra. The parameter space in Figure 13 indicates where minerals with hydration features (Table S1) occur when present as pure phases. Spectra with positive R5/R6 (937 nm/1013 nm) ratios (indicative of a >980 nm absorption) and R3/R5 (805 nm/937 nm) ratios close to 1.0 (indicative of otherwise flat NIR profiles) are consistent with – but not unique signatures of – some hydrated minerals (e.g., gypsum and epsomite, Figure 7). These spectral characteristics are also easily masked in mixtures with other phases, so detecting hydration in Mastcam spectra is expected to be challenging.

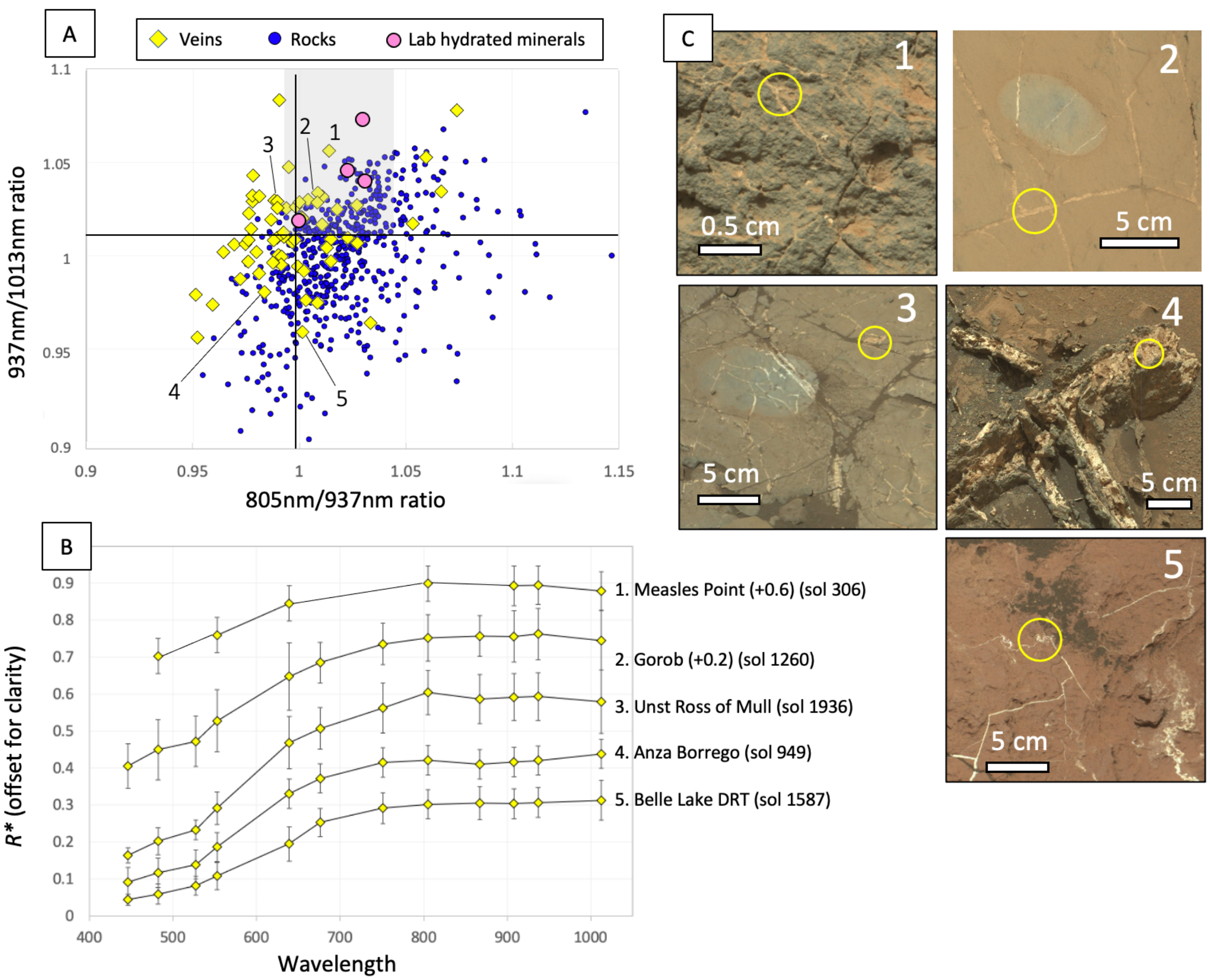

Figure 13. *(a) Spectral parameters that can distinguish minerals with hydration absorptions >980 nm, shown for lab spectra of hydrated minerals convolved to Mastcam bandpasses (pink circle, full spectra shown in Figure 7), Mastcam vein targets (yellow diamonds), and all other rock targets (blue dots). The gray region indicates where hydrated minerals fall in this parameter space; (b) Example Mastcam spectra from a variety of vein morphologies (note that the Measles Point observation only included filters R0345); (c) Mastcam R0 images of veins, spectra were extracted from ROIs within the yellow circles.*

.

Vaniman et al. (2013) reported possible hydration in veins near the landing site, and ChemCam H data suggest the calcium sulfate veins are predominantly bassanite, with some gypsum and anhydrite (Nachon et al., 2014; Rapin et al., 2016). We do not find evidence for hydration in Mastcam spectra of the veins to be widespread across the traverse. We find that spectra of light-toned, fracture-filling veins (yellow diamonds, Figure 13) do not cluster within the region of the parameter space that is consistent with hydrated minerals, which we would expect if the veins were dominated by hydrated phases such as gypsum. Rather, vein spectra have a spread of values, indicating variability within these features. While some vein spectra do exhibit R6 (1013 nm) absorptions, which may be consistent with hydration, these spectra were collected from ROIs containing only a few pixels and therefore suffer from high uncertainty due to the factors discussed above. The multispectral database only includes spectra from a subset of vein targets, owing to their small sizes and the difficulty in extracting spectral averages; however, adding more of the narrow veins to the database and classifying their textures (such as thin, thick, boxwork, subparallel, or "chickenwire"; e.g., Minitti et al., 2017) will be part of ongoing database development.

3.2 Soil Spectral Variability

Soils across Curiosity's traverse show notable spectral trends with elevation (Figure 14). For spectral parameters related to iron-bearing phases and ferric materials, the soil variability across the traverse does not follow the variability seen in adjacent rocks. At the landing site and Yellowknife Bay, the soils are remarkably redder and have deeper L1 (527 nm) band depths than the rocks, a trend that reverses later in the traverse. At low elevations, the L1 (527 nm) band depth, L3/2 (751 nm/445 nm) ratio, and L6/L3 (1012 nm/751 nm) ratio parameters increase from the landing site through the Bradbury Group and into the lower Mount Sharp Group members. At elevations above -4450 m (in the Karasburg member and above), these parameters remain low, including in regions where the rock spectra vary considerably in the Sutton Island, Pettegrove Point and Jura members. Anomalously low L6/L3 (1012 nm/751 nm) ratios are seen at specific elevations within the Hartmann's Valley (-4430 m) and Sutton Island members (near -4300 m), corresponding with Curiosity's exploration of the Bagnold Dune field in these locations. The low red/blue ratio and L6/L3 (1012 nm/751 nm) ratios at these elevations are spectrally consistent with olivine (see Section 4).

The L5 (867 nm) band depth in soils is less variable than other parameters across the full traverse (Figure 14), with values restricted between -0.04 and 0.05 (compared to the range of -0.06 to 0.17 in rock spectra). At lower elevations, this band depth parameter is slightly negative, then slightly positive from the Karasburg to Pettegrove Point members, after which values are near zero. In the Blunts Point and Jura members, where the deepest L5 (867 nm) band depths are observed in rock spectra, the soils consistently have flat NIR profiles (e.g., Figure 14).

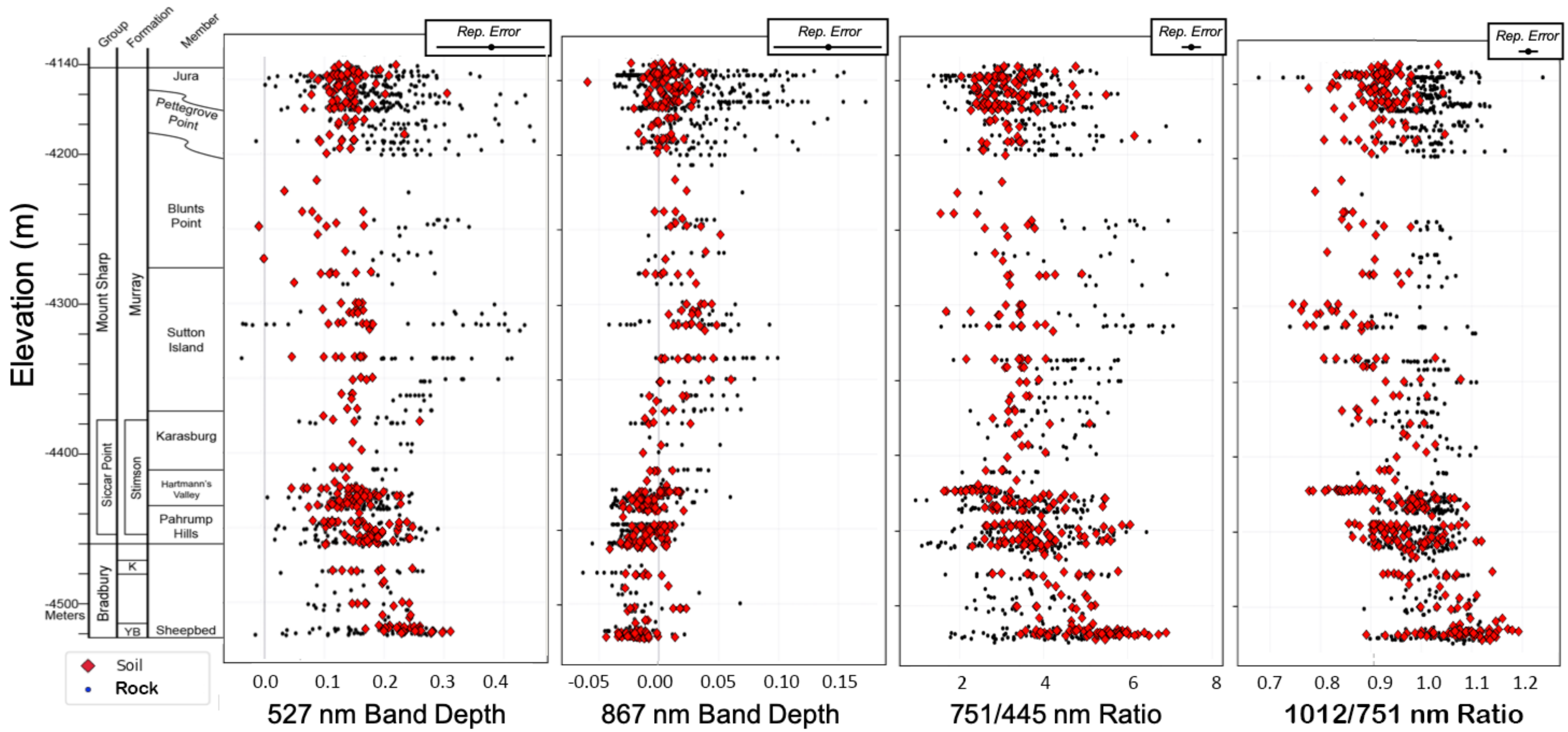

Figure 14. *Soil spectral parameters (red diamonds) compared to rock spectral parameters (black dots) across the traverse. Parameter definitions provided in Table 4.*

3.3 Influence of Atmospheric Opacity

To investigate the potential influence of atmospheric events on the spectral trends presented above, we searched for correlations between atmospheric dust opacity (tau) and a variety of spectral parameters. Figure 15 shows the "redness" as the L3/L2 (751 nm/445 nm) ratio for dusty soil and rock spectra across the traverse (which should be less spectrally variable than disturbed soils, DRT targets and drill fines, due to the masking effects of dust), with regions highlighted where tau exceeded 1.0. If redder illumination from atmospheric dust loads had influenced Mastcam spectra, we would expect to see enhanced reddening in the spectra of both soils and rocks during high-tau periods. However, we do not observe increased L3/L2 (751 nm/445 nm) ratios corresponding to the high-tau excursions, including the Mars Year 34 (2018) global dust storm.

The 2018 dust storm originated around sol 2060, reached Gale crater 15 sols later, and did not decline to climatological values until ~sol 2157 (Guzewich et al., 2019; Viúdez-Moreiras et al., 2019). Dust storms of this magnitude periodically sweep the surface of Mars, and during the preceding 2007 event, MER Opportunity observed albedo increases in Pancam's broadband (L1 filter) observations due to the resulting redder illumination conditions (Rice et al., 2018). However, the Mastcam observations acquired during similar high-tau conditions were not systematically brighter or redder than during low-tau periods (Figure 15), suggesting that Mastcam's radiometric calibration mitigates the influence of redder illumination. Comparisons of spectra of the same rock targets before and after the dust storm also show no significant changes (Jacob et al., 2020). These observations provide confidence that the observed variations in soil and rock spectra, as discussed in Sections 3.1-3.2 above, are due to real compositional variations.

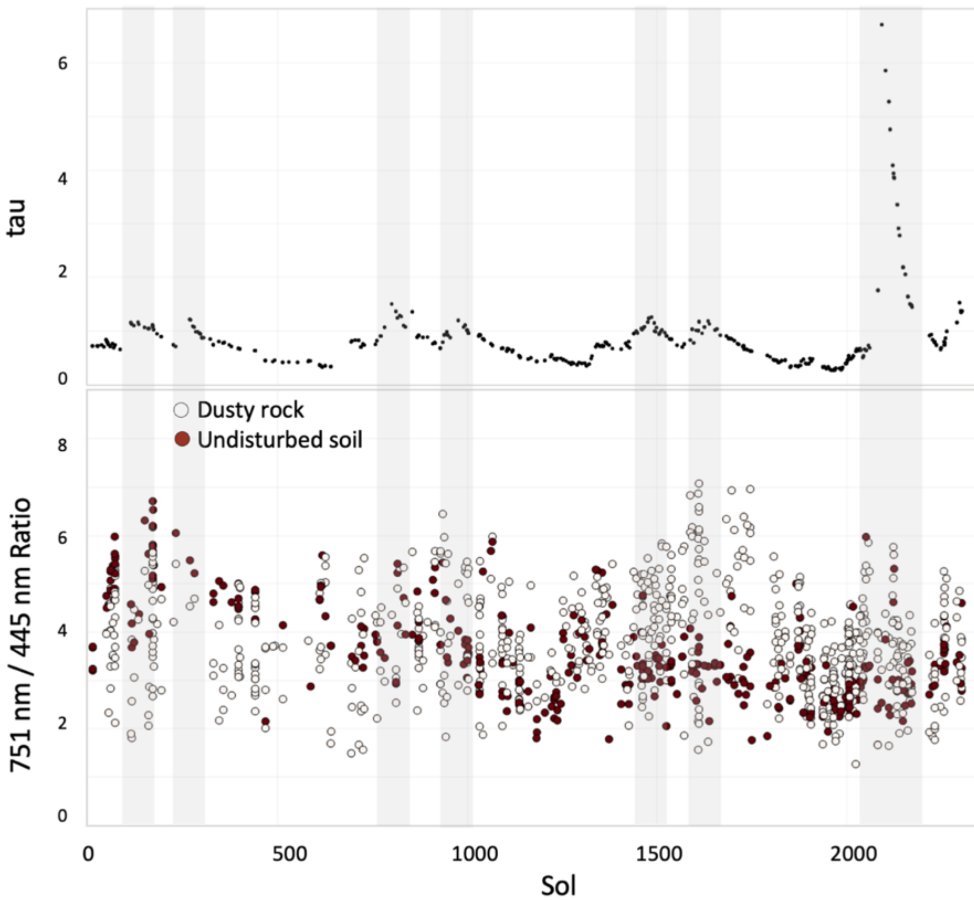

Figure 15. *Comparison of atmospheric dust opacity (tau) to the redness of dusty rocks and soils across the traverse. Above: tau vs. sol, showing the MY34 global dust storm as the spike around sol 2060. Below: 751 nm / 445 nm ratio for dusty rocks and undisturbed soils across the traverse. Gray regions indicate sol ranges where tau > 1.0.*

3.4 Principal Components Analysis

Table 5 summarizes results of the PCA for rock and soils. In the resulting principal component (PC) coordinate spaces, the greatest variance lies along the first principal component (PC1), the second greatest variance lies along PC2, etc. The majority of spectra have low values of all PCs, and spectra with the highest vs. lowest PC values are representative of the spectral characteristics that define the highest-order variability of the dataset. Below we discuss the characteristics of spectral endmembers identified in these analyses (Table 5), which we use to help identify spectral classes (as discussed in Section 4.1).

Table 5. *Principal components of rock and soil spectra, with observations from which the maximum and minimum PC examples in Figures 16 and 20 are taken.*

	PC	% Variance	Defining Spectral Characteristics	Max PC Examples	Min PC Examples
Rocks	1	72.06	Overall redness (751nm/445nm ratio)	Big Sky Post Sieve Pile (sol 1138); Quoddy Quimby (sol 1608); Lubango Full Drill (sol 1321); Greenhorn Full Drill (sol 1138)	Perry (sol 1610); Quoddy Quimby (sol 1608); Ailsa Craig Drill Tailings (sol 2123); Belle Lake DRT (sol 1587)
	2	17.84	Relative blue reflectance (527nm/445nm ratio); position peak NIR reflectance between 751-937nm	Sutton Island Manset (sol 1524); Zephyr Ledges (sol 1790); Benbecula (sol 1964)	Confidence Hills Drill Tailings (sol 762); Confidence Hills Dump Pile (sol 782); Oudam Drill Tailings (sol 1363); Inverness Drill Tailings (sol 2171)
	3	5.91	867 nm band depth and 527nm band depth	Walls Peninsula Stereo (sol 2007); Britt Stereo (sol 2036); Voyageurs Drill Tailings (sol 2113); Woodhill (sol 2255); Stranraer DRT (sol 2007)	Gariep (sol 1314); Meob DRT (sol 1349); Askival (sol 2016); Windjana DRT (sol 626)
	4	1.62	Position of peak NIR reflectance at 751 nm vs 805 nm	Windjana Dump Pile (sol 705); Seely (sol 999); Durness Stereo (sol 1996); Sutton_Inlier (sol 174)	Blinkberg Stereo (sol 1850); Gometra (sol 2259); Marimba Drill Tailings (sol 1421)
Soils	1	79.35	Overall redness (751nm/445nm ratio)	Ekwir (sol 150); Wernecke (sol 172); John Klein Dill Tailings (sol 183); Pearson (sol 66)	Gobabeb Dump Pile (sol 1229); Hildreths (sol 1637); Zephyr Ledges (sol 1790); Hoanib (sol 1182)
	2	13.23	Position of peak NIR reflectance at 751 nm vs 805 nm; concavity of NIR profile	Matagamon (sol 1603); Ogunquit (sol 1652); Greening Island (sol 1571)	Kubib (sol 1183); Aubures (sol 1368); Ile Damour (sol 1749)
	3	3.31	638nm to 805nm concavity; filter-to-filter NIR variability	Duck Brook Bridge DRT (sol 1682); Winter Harbor DRT (sol 1737); Fort Brown DRT (sol 1876); Belle Lake DRT (sol 1587)	Jemtland (sol 1608); Mark Island (sol 1729); Inverness (sol 2217); Telegraph Peak Tailings (sol 909)
	4	2.14	527nm band depth; 908nm band depth	Broad Cove (sol 1703); Fernald Point wheel track (sol 1728); Long-dist VRR (sol 1745); Eddie Brook (sol 1688)	Goulburn (sol 13); Copper Canyon wheel track (sol 728); Hoanib (sol 1182)

3.4.1 Rocks

In our rock analysis, 72% of the variance lies in PC1, 18% in PC2, 6% in PC3, 2% in PC4, and 2% in all remaining components (Table 5). Coordinate spaces for the first four components are shown in Figure 16, with each point representing a single rock spectrum from the database, color-coded by stratigraphic member. Some trends with lithology are immediately apparent: the Stimson DRT targets and drill fines are distinct from the rest of the dataset in PC1 vs. PC2, and have positive values of PC3. Also, the Kimberley DRT targets and drill fines all have negative values of PC3 and positive values of PC4, distinct from the rest of the dataset.

Figure 17 includes examples of spectra with minimum and maximum component values for PCs 1-4. Based on these representations, PC1 corresponds to the overall "redness" of rock spectra, and the distinguishing metric for these spectra is the L3/L2 (751 nm/445 nm) ratio. PC2 characterizes the peak NIR position, which occurs closer to 751 nm in the maximum PC2 examples and longward of 900 nm in the minimum PC2 examples. The brightness of the blue filters contributes to this component as well, as the minimum PC2 values all have high reflectance values as 445 nm and 438 nm. We find these short wavelength "upticks" exclusively in drill fines (see minimum PC2 and maximum PC1 examples), and they may be related to previously-reported "blue artifacts" of unknown origin (Wellington et al., 2017).

The maximum and minimum examples of PC3 (Figure 17) show that this component is related to the shape of the NIR profile: the maximum PC3 examples have the strongest L5 (867 nm) absorption bands, while the minimum PC3 examples have convex NIR profiles (negative L5 (867 nm) band depths). The spectral contributors to PC4 are difficult to identify in their end member spectra, although the spectra in the maximum vs. minimum PC4 examples share common positions for peak NIR reflectance at L3 (751 nm) vs. R3 (805 nm), respectively.

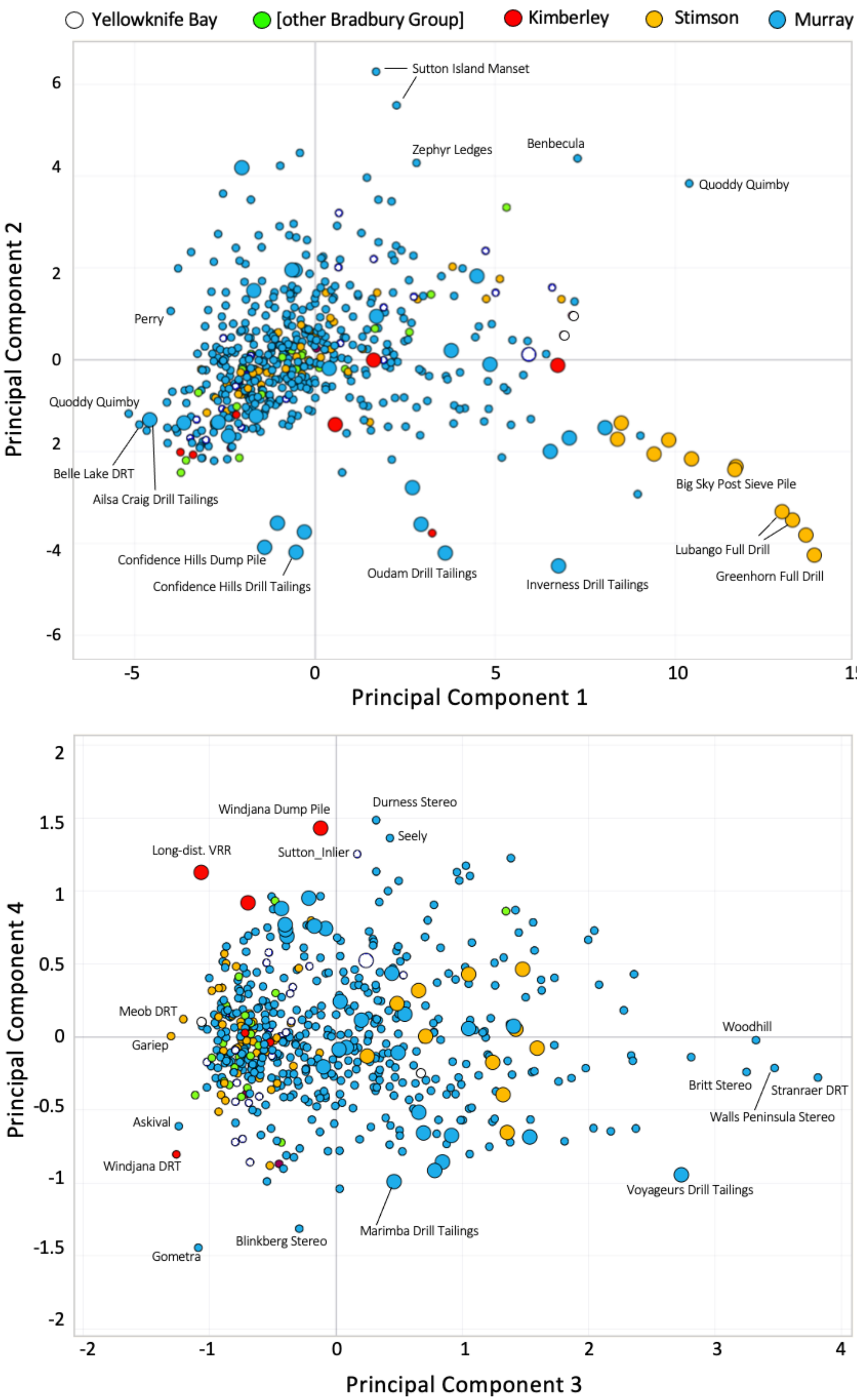

Figure 16. *Principal component plots for rocks in the multispectral database. Large circles are low-dust surfaces (drill fines, DRT targets and broken rocks), and small circles are dusty rocks. Colors indicate formations within the Bradbury Group (Yellowknife Bay, Kimberley and others) and Mt. Sharp Group (Stimson and Murray).*

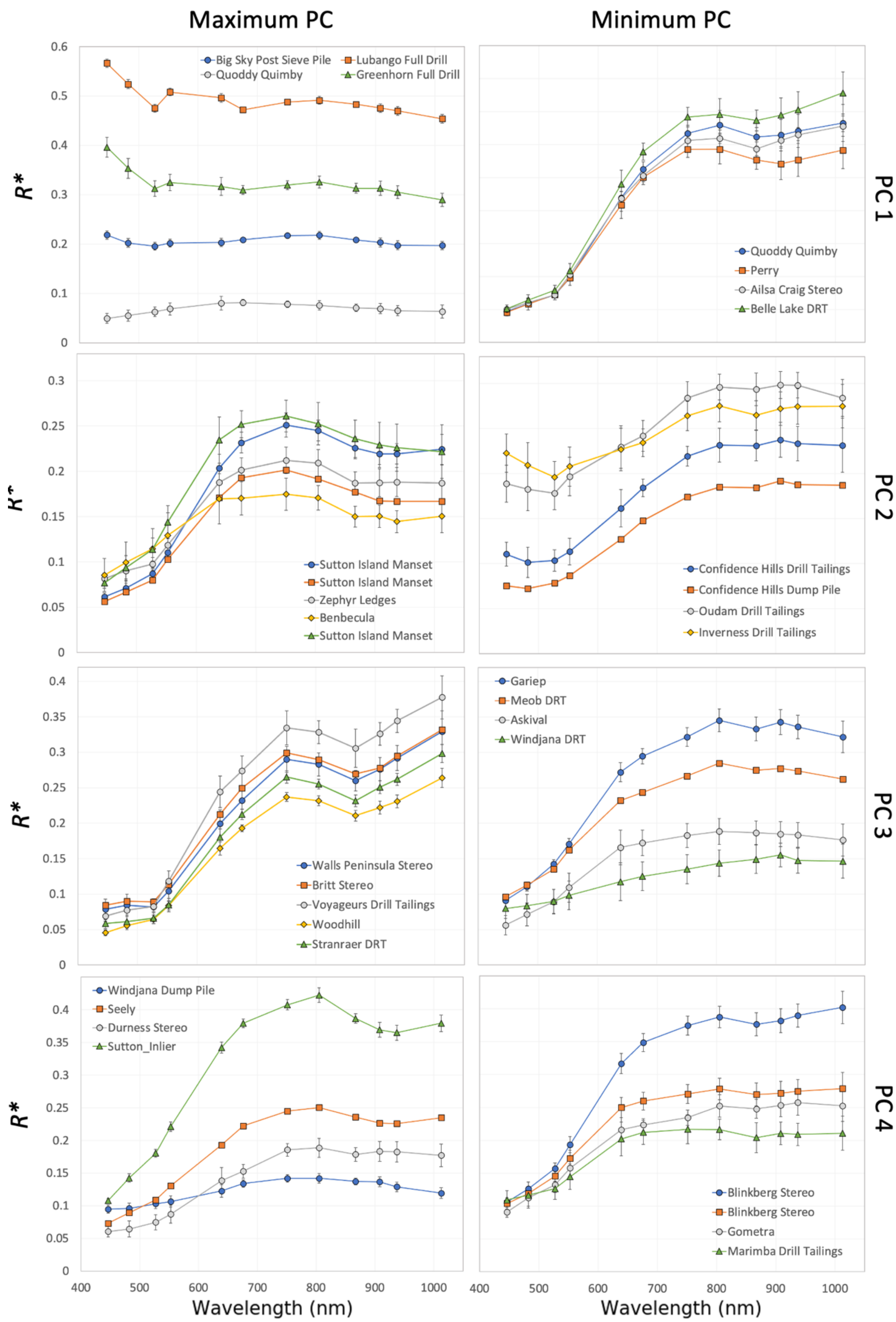

Figure 17. *Example rock spectra with maximum and minimum values of each of the first four principal components. Observation details provided in Table 5.*

3.4.2 Soils

In our soil analysis, 79% of the variance lies in PC1, 13% in PC2, 3% in PC3, 2% in PC4, and 3% in all remaining components (Table 5). Coordinate spaces for the first four components are shown in Figure 18, with each point representing a single rock spectrum from the database color-coded by elevation. The component space for PC2 vs. PC1 shows clear trends with elevation: spectra from soils at the very lowest elevations have the smallest PC1 values. Soil spectra from a broader range of elevations below -4400 m have low PC3 values, and those with the highest PC4 values are from elevations above -4300 m. Spectra from soils on Vera Rubin ridge, at the highest elevations in the dataset, mostly have values near zero for all PCs.

Figure 19 shows examples of spectra exhibiting minimum and maximum component values for PCs 1-4. Based on these representations, PC1 corresponds to overall "redness" of soil spectra (similar to PC1 for rock spectra), as characterized by large L3/L2 (751 nm/445 nm) ratios vs. flat spectral profiles. PC2 relates to the position of the peak NIR reflectance (closer to 751 nm for maximum PC2 vs. 805 nm for minimum PC2) and the concavity of the NIR profile. The contributing spectral features to PCs 3 and 4 are less clearly identified from maximum and minimum end member spectra. PC3 may be related to the concavity of the NIR profile between 638nm to 805nm and a "sawtooth" pattern in the NIR bands (likely an artifact from joining the left- and right-Mastcam spectra, see Section 2.7). PC4 may be related to the L1 (527nm) band depth and R4 (908nm) band depth (exemplified in example spectra from Goulburn for minimum PC4).

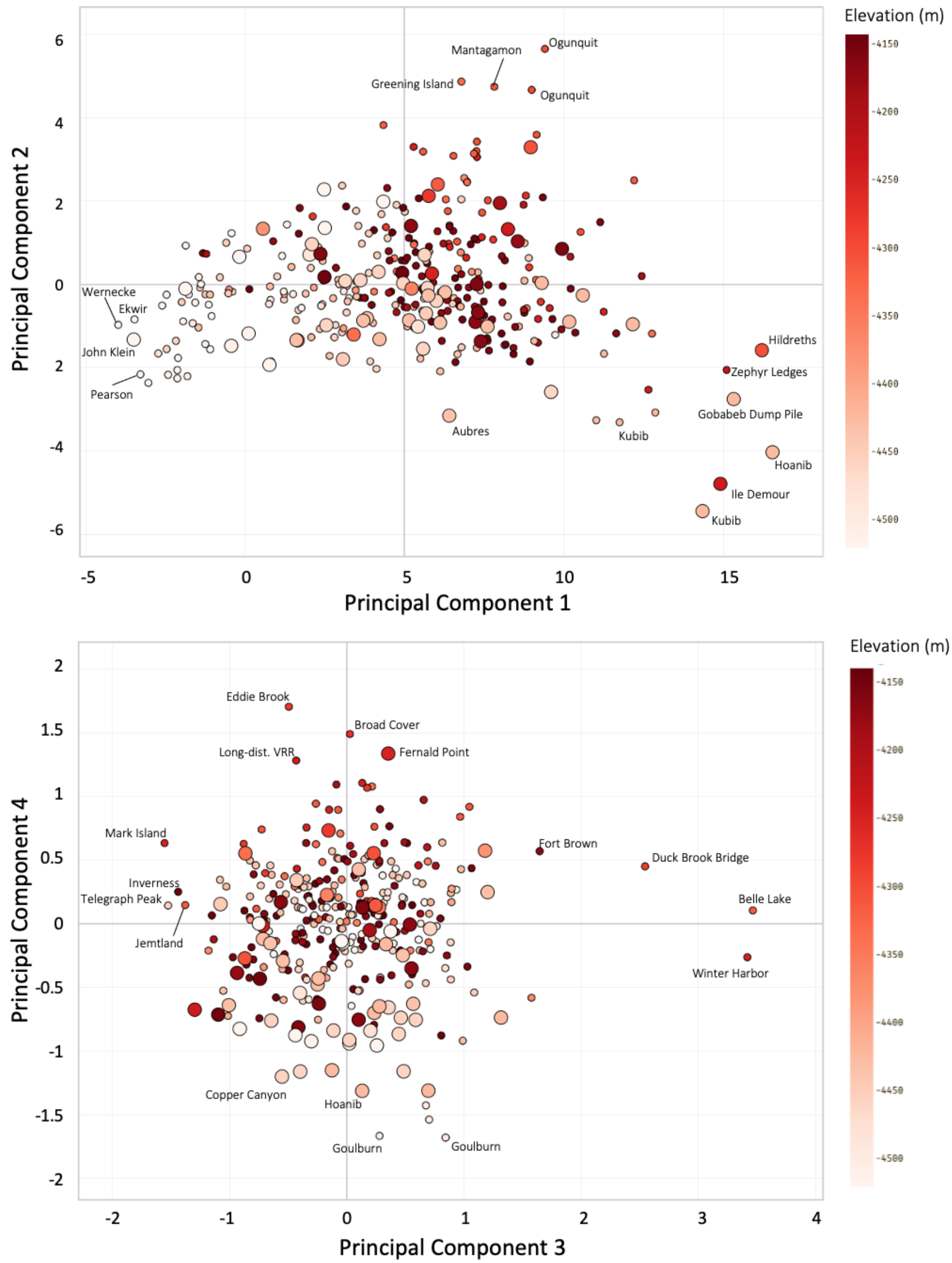

Figure 18. *Principal component plots for soils in the multispectral database. Large circles are disturbed surfaces (e.g., wheel tracks), and small circles are dusty soils. Color scale indicates elevation along the traverse, with lighter shades corresponding to lower in the stratigraphic section (earlier in the mission), and darker shades corresponding to higher in the section (later in the mission). Labeled points indicate spectra included in Figure 19.*

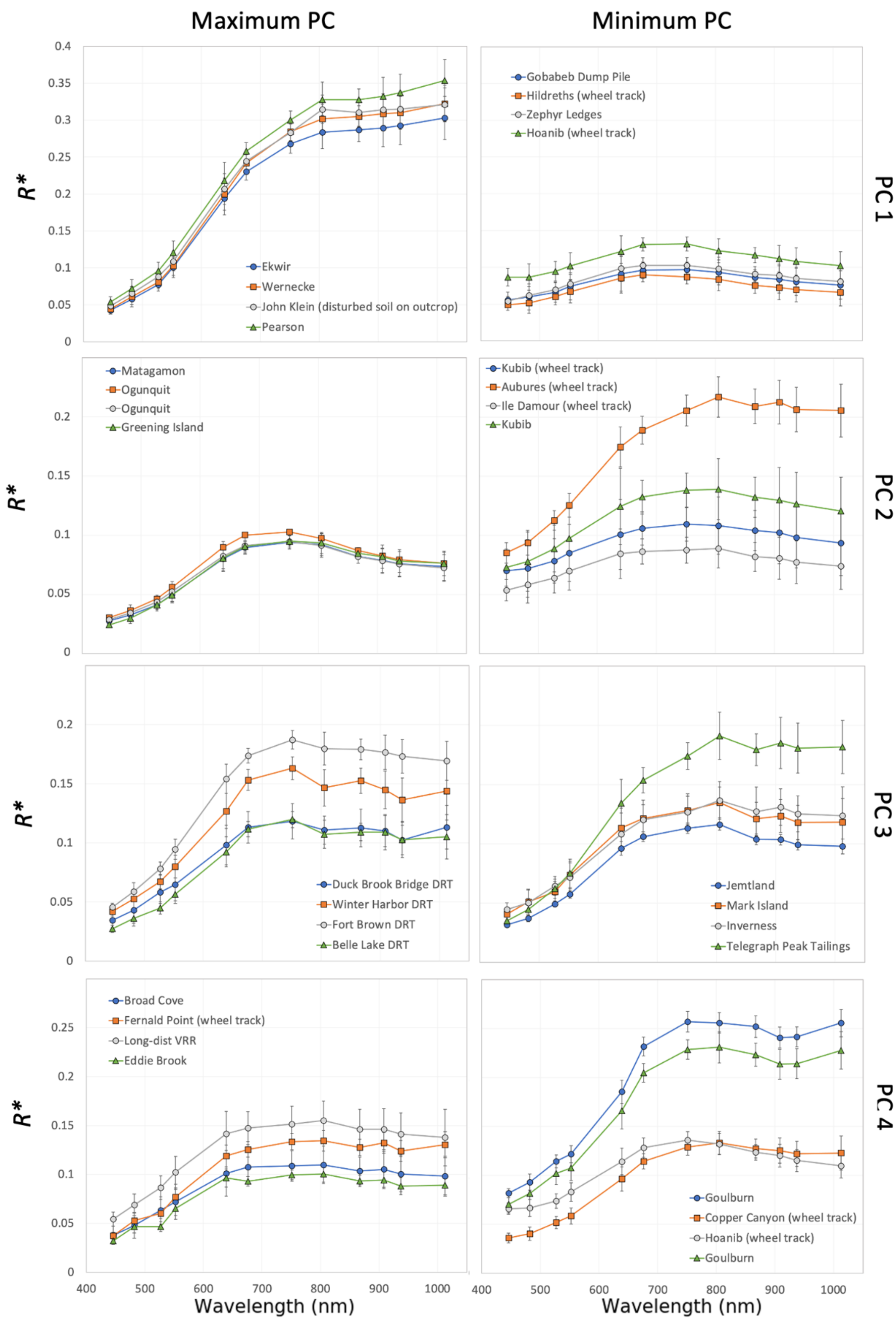

Figure 19. *Example soil spectra with maximum and minimum values of each of the first four principal components. Observation details provided in Table 5.*

4 Discussion

4.1 Mastcam Spectral Classes

4.1.1 Rock Classes

Synthesizing the results above, we propose nine major spectral classes for rock targets within the Mastcam multispectral database (Table 6). Figure 20 shows type examples of these rock spectral classes, with class names given for notable rock targets (either DRT targets, drill targets, or the first target of the class that Mastcam observed). Class numbers correspond to the prevalence of spectra in our database. The most common spectral class across the traverse is Class 1 (Neutral/Dusty), characterized by moderate to large red ratios and flat NIR profiles. These spectra do not have any of the extreme endmember spectral characteristics of the PCs in Figure 16. The redder Neutral/Dusty Class spectra are consistent with dust (e.g., see the nanophase hematite spectrum in Figure 6), and the variability of spectra within this class likely corresponds to different amounts of dust cover above rock surfaces with generally featureless NIR spectra. Thus, the Neutral/Dusty Class includes rocks with a range of compositions and origins. In addition to very dusty surfaces, some spectra of dust-cleared rocks and drill fines from each stratigraphic member fall into this class as well, including all DRT targets within the Stimson formation. Spectra of fracture-filling, Ca-sulfate veins, which are high-albedo with generally flat NIR profiles and red VIS profiles (e.g., Figure 13), fall within the Neutral/Dusty class as well.

Class 2 (Marimba) spectra are defined by moderate red ratios and weak absorptions at L5 (867 nm), consistent with varying contributions of hematite and/or other Fe-oxides. Class 3 (Sutton Island Manset) spectra are associated with dark diagenetic features, one of three spectral types within Sutton Island noted by Haber al. (2020) (the other two of which, based on our classification schemes, would be grouped within the Marimba and Hexriver Classes identified here). Class 4 (Hexriver) spectra exhibit the strongest L5 (867 nm) and L1 (527 nm) band depths, consistent with red fine-grained hematite. These four most abundant classes encompass the majority of rock spectra within the Sutton Island member and at higher elevations in the traverse.

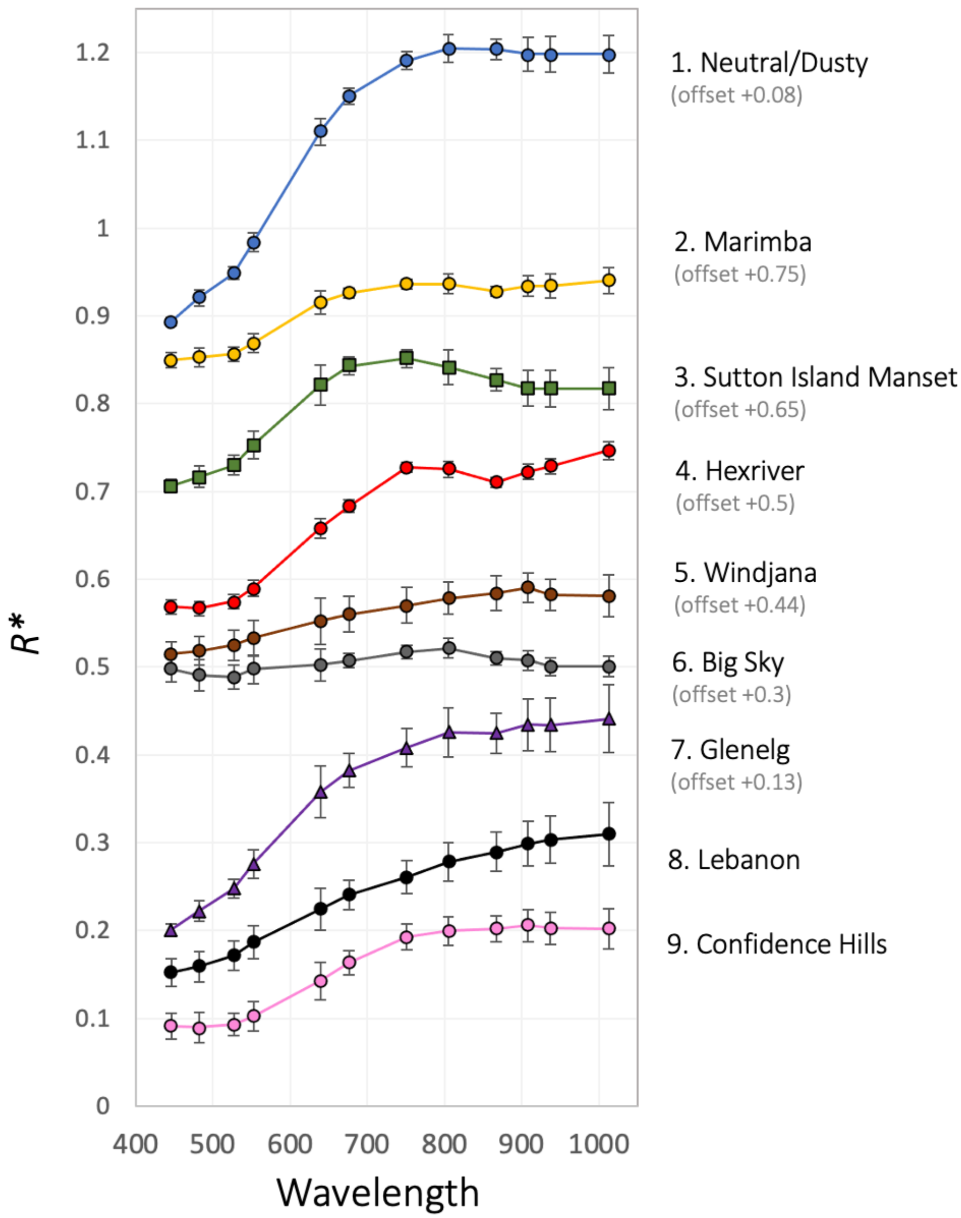

Figure 20. *Representative spectra from each of the nine rock spectral classes. Spectra are from observations listed in Table 6.*

Table 6. *Summary of rock spectral classes.*

Class	Name	Short Description	Defining Spectral Characteristics	Type Examples	Distribution	Interpretation
1	**Neutral/Dusty**	Red, flat NIR profile	Moderate 751nm/445nm ratios; Small values of 1012nm/751nm ratio; Flat NIR profiles	sol 183, mcam00993	Consistent throughout the traverse	Variable amounts of dust upon rocks with neutral spectra
2	**Marimba**	Red, shallow 866nm band	Large 751nm/445nm ratios; Small values of 1012nm/751nm ratio; Positive 867nm band depths	sol 1425, mcam07034	Prevalent in the Murray formation, mostly above the Hartmann's Valley member	Rocks bearing some hematite, but less than the Hexriver class
3	**Sutton Island Manset**	Gray, Negative NIR slope	Peak reflectance at 751nm; Small 1012/751nm ratios; Positive 867nm band depths	sol 1524, mcam0770	Primarily within the Sutton Island member	Dark, diagenetic features, possibly nontronite-bearing
5	**Hexriver**	Red, deep 866 nm band	Large 867nm and 527nm band depths	sol 1885, mcam09853	Mostly within the Sutton Island and Jura members, with significant local variability	Hematite-bearing, strongly diagenetically-altered rocks
5	**Windjana**	Gray, convex NIR profile	Straight, flat to positively sloping profiles to 908nm; 908nm/1013nm < 1.0	sol 626, mcam02676	Primarily within the Kimberley formation and Pahrump Hills member	Rocks with variable contributions of dark Fe- and/or Mn-oxides
6	**Big Sky**	Gray, flat NIR profile	1012nm/751nm ratios close to 1.0; blue/red ratios positive or close to 1.0	sol 1120, mcam04990	Drill fines, mostly within the Stimson formation	Rock interiors with minimal Fe-oxides
7	**Glenelg**	Red, positive NIR slope	Large 751nm/445nm ratios; Positive 1012nm/751nm ratios; no 867nm band depth	sol 069, mcam00486	Only seen within Bradbury Group	Thick dust cover on rock surfaces
8	**Lebanon**	Gray, positive VIS and NIR slope	1012nm/751nm ratios > 1.1; 741nm/527nm ratios 1.0-2.0	sol 640, mcam02718	Isolated float rocks, found sporadically at all elevations	Iron meteorites
9	**Confidence Hills**	Gray, peak at 908nm	Large 527nm band depth; flat NIR profile	sol 758, mcam03257	Only seen within Pahrump Hills member	Dark Fe-oxide, possibly coarse-grained hematite

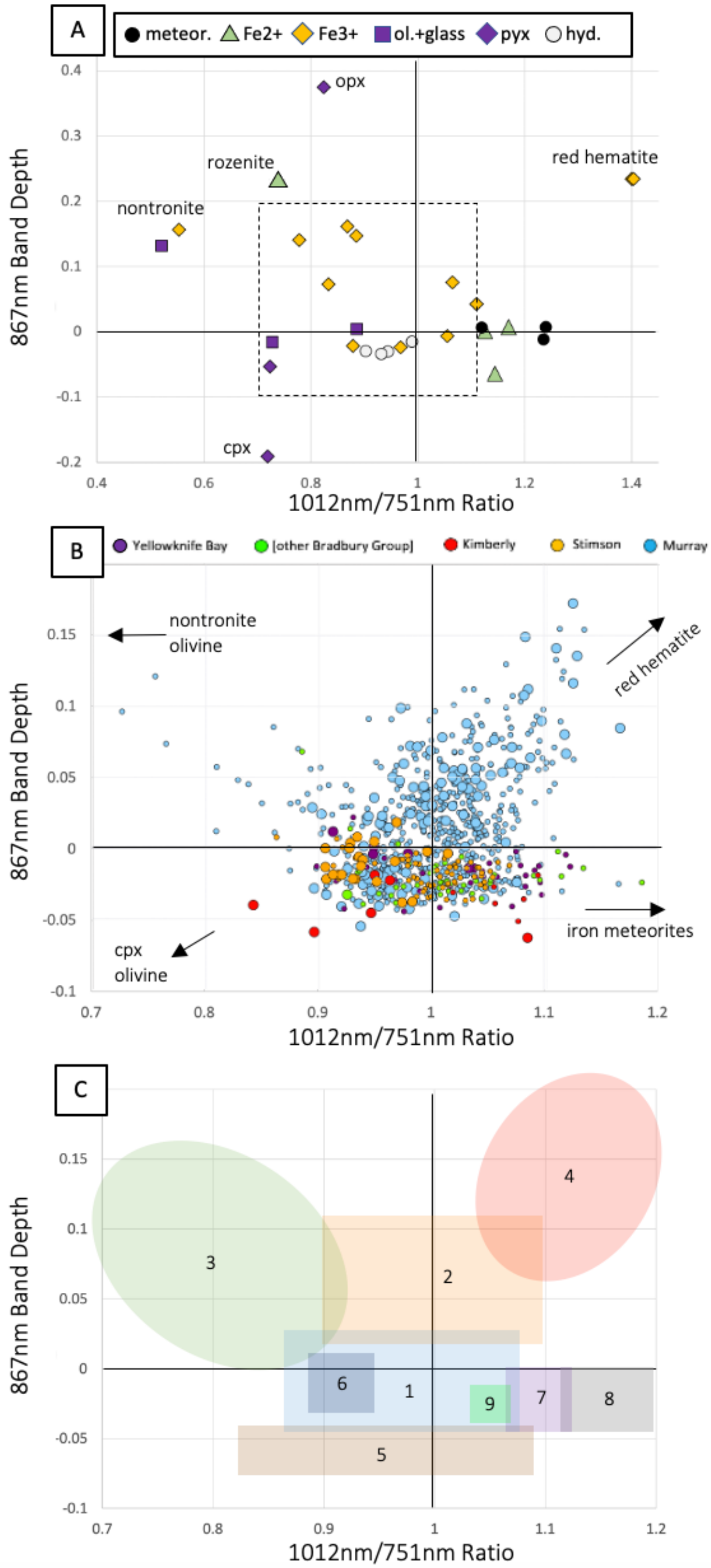

Figure 21. *The spectral parameters that best distinguish rock spectral classes are the L5 (867 nm) band depth vs. L6/L3 (1012 nm/751 nm) ratio, shown for: (a) Laboratory spectra of*

minerals convolved to Mastcam bandpasses: ferrous alteration phases (green triangles); pyroxenes (purple diamonds); olivines and basaltic glass (purple squares); ferric alteration phases (orange diamonds); iron meteorites (black circles), and hydrated minerals (white circles). Full spectra shown in Figures 6-7. The region bounded by the dashed line is that shown in b-c; (b) All Mastcam rock spectra, color coded by stratigraphic formation; (c) Rock spectral classes (names and descriptions of which are provided in Table 6).

At lower elevations, Mastcam observed several spectral classes that are largely confined to specific stratigraphic members and have rarely been encountered since. Class 5 (Windjana Class) targets include dark rocks and drill fines in the Kimberley formation, where Mn-oxides occur as subparallel fracture fills (Lanza et al., 2015). These dark oxides are the likely cause of this class' defining spectral characteristics (Table 6), most notably the straight, flat to positively sloping profiles out to 908nm. Class 6 (Big Sky) spectra are remarkably flat across the full Mastcam wavelength range. The predominant targets within this class are drill fines within the Stimson formation, corresponding to sandstone rock interiors with little Fe-oxides. Class 7 (Glenelg) spectra are characterized by flat and positively-sloping NIR profiles.

Class 8 (Lebanon) includes candidate meteorites, as defined by their positively sloping spectral profiles across the full wavelength range (as defined by the parameters shown in Figure 14). The meteorites detected by Curiosity are dominantly iron-nickel and stony iron types, which may be more abundant, more resistant to erosion, and/or more easily spotted than chondritic meteorites (Wellington et al., 2018). Stony meteorites may also not be spectrally distinguishable from other rocks in Gale crater, and if present may be lumped into another of the rock spectral classes. The least abundant rock spectral class, Class 9 (Confidence Hills), is specific to drill fines and DRT targets near Confidence Hills. We identified this class as distinct from other spectra by their minimum values of PC2, which are defined by large L2 (527 nm) band depths and flat NIR profiles.

The spectral parameters that best separate these classes are the L5 (867 nm) band depth and the L6/L3 (1012 nm/751 nm) ratio. Figure 21b shows the distribution of all rock spectra in this parameter space, with regions that each rock class occupies shown in 21c. Note that the defining spectral characteristics of Class 6 (Big Sky) and Class 9 (Confidence Hills) are not captured by these parameters, so they overlap with the Class 1 (Dusty/Neutral) region in this parameter space. In comparison to the distribution of convolved laboratory spectra in this parameter space (Figure 21a), we interpret that Class 3 (Sutton Island Manset) spectra are most consistent with nontronite and/or olivine phases, Class 5 (Hexriver) spectra are consistent with red hematite, and reaffirm that Class 8 (Lebanon) spectra are consistent with iron meteorites. We note that no rock spectra in the database fall within the lower left corner of this parameter space, indicating that no spectral class is dominated by clinopyroxenes or other phases with convex NIR profiles.

The distribution of spectral classes with elevation (Figure 22) reveals that some – but not all – spectral rock classes are associated with specific formations in the stratigraphy. The Neutral/Dusty Class is the only class that Curiosity has encountered at nearly every elevation interval; this is unsurprising, given that this class lumps together a variety of feature types (e.g., dusty rocks, DRT targets, diagenetic veins) and compositions that lack distinguishing spectral characteristics to Mastcam. The Lebanon Class occurs at punctuated elevation intervals, and indeed we would expect a seemingly-random distribution of iron meteorites throughout the stratigraphy. The remaining seven rock classes, however, tell a story of changing spectral characteristics across Curiosity's traverse.

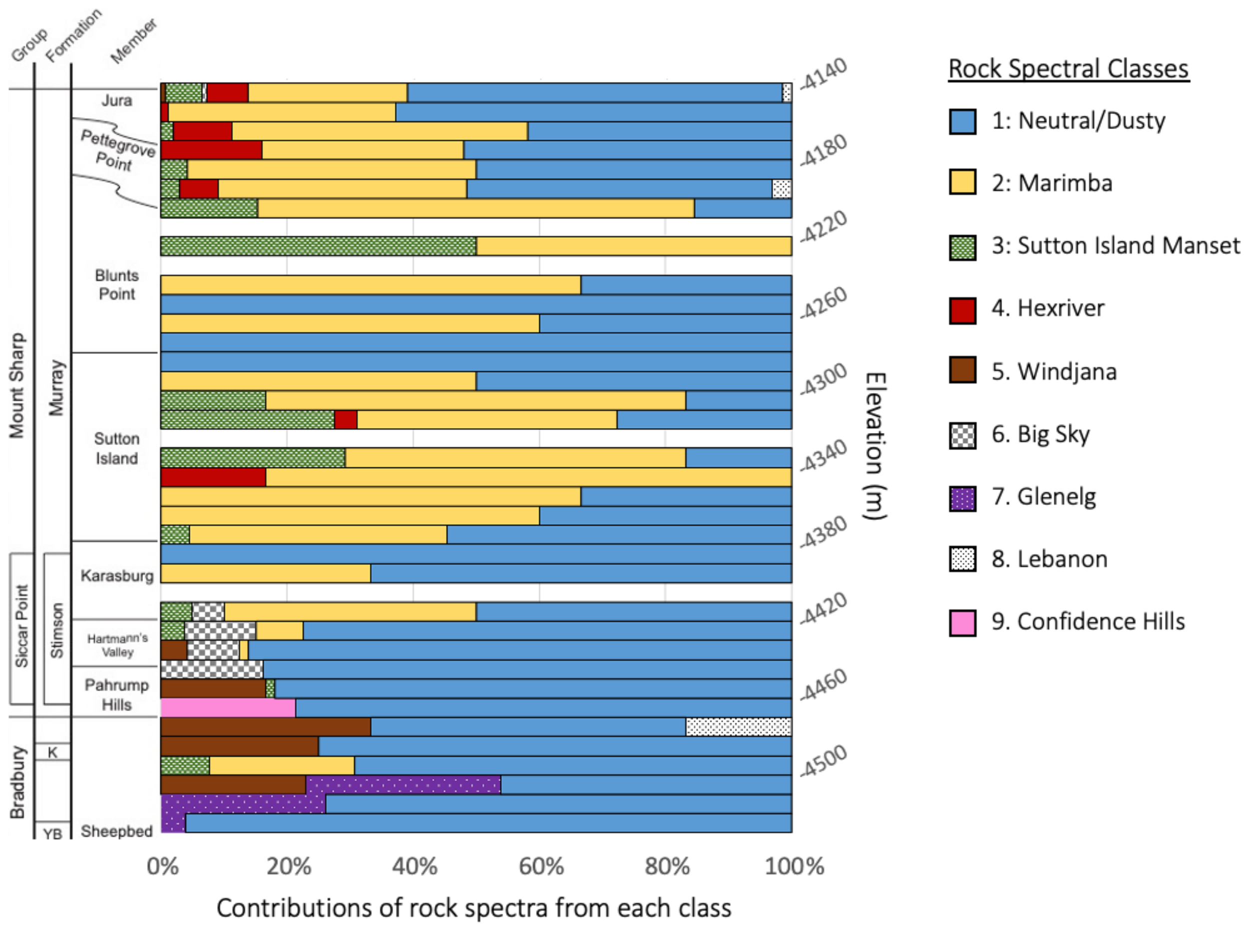

Figure 22. *Distribution of rock spectral classes with elevation across Curiosity's traverse. Data are binned to 10 m elevation intervals. Percentage values indicate proportions of rock spectra belonging to each class within the elevation bin (numbers of spectra provided in Table S4).*

Collectively, these correlations with stratigraphy show that many of the rocks that Curiosity studied within the Bradbury Group are spectrally distinct from those of the Mt. Sharp Group; the Fe-oxides influencing the positively-sloping NIR profiles of the Glenelg Class spectra are different from those causing the pronounced L5 (867 nm) bands in the Marimba and Hexriver Classes (red hematite). Within the Mt. Sharp Group, the Stimson formation drill tailings lack any spectral indication of Fe-oxides and are spectrally distinct from the Murray formation drill tailings and other rocks. The confinement of the Hexriver Class to the Sutton Island, Pettegrove Point and Jura members of the Murray formation indicates that rocks in these intervals are most strongly influenced by the presence of fine-grained red hematite (which is also supported by CRISM observations; Fraeman et al., 2020b). Within the Sutton Island member, the predominance of the Sutton Island Manset Class at some elevations indicates an increasing influence of dark, possibly nontronite-bearing diagenetic features (Haber et al., 2020), which return in Blunts Point.

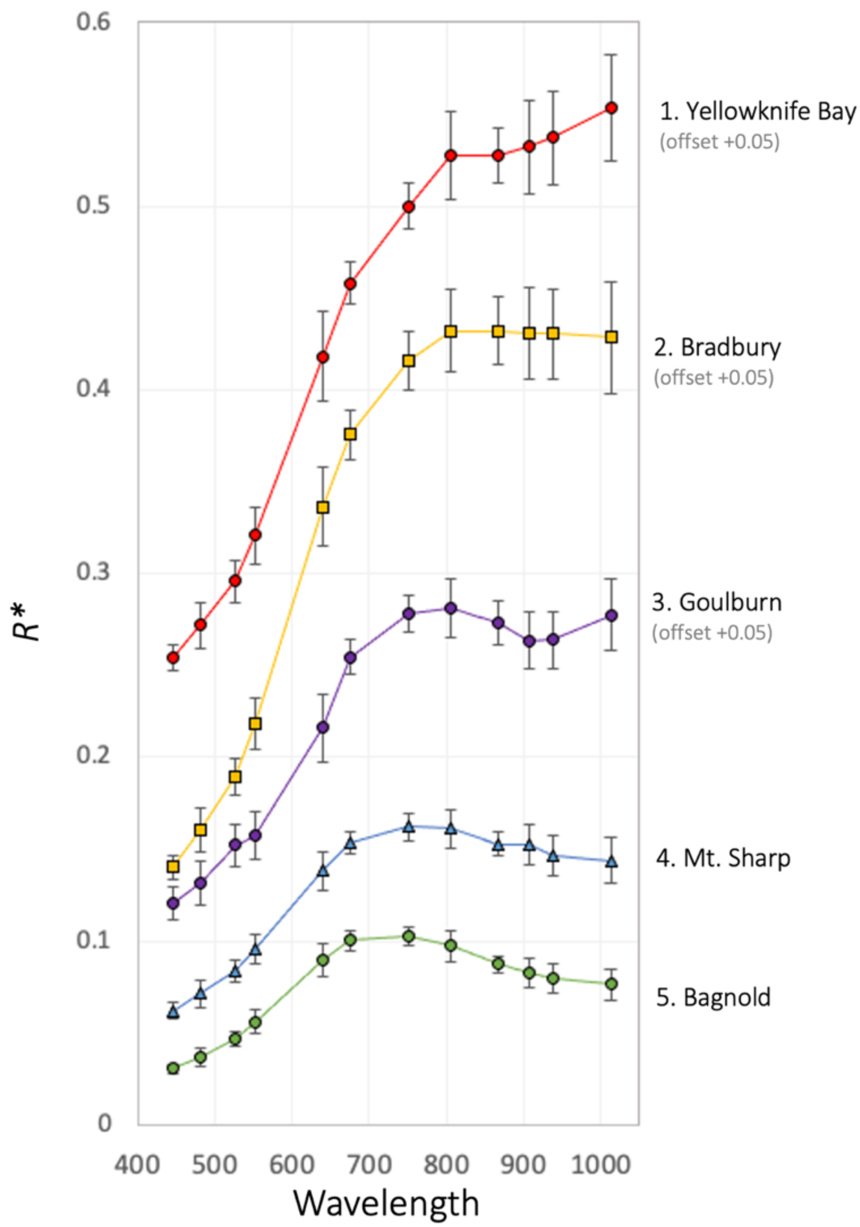

Figure 23. *Representative spectra from each of the five soil spectral classes. Spectra are from observations listed in Table 7.*

4.1.2 Soil Classes

Based on PCA and spectral parameter analyses, we have identified five spectral classes of soils in the multispectral database. Type examples of these classes shown in Figure 23, and their spectral characteristics are summarized in Table 7. Classes are numbered in order of decreasing "redness" (Class 1 having the largest L3/L2 (751 nm/445 nm) ratios), and class names are given for the region of the traverse where each soil class is most prevalent. Class 1 (Yellowknife Bay) soil spectra are also distinct in their positively-sloping NIR profiles, which are consistent with Fe-oxides. While similar to Goulburn Class soil spectra (Figure 19), the Yellowknife Bay Class soil spectra are generally redder (larger L3/L2 (751 nm/445 nm) ratios) and have larger L6/L3 (1012 nm/751 nm) ratios. Class 2 (Bradbury) spectra are characterized by flat NIR profiles, similar to the Dusty/Neutral Class of rock spectra, but generally redder in VIS wavelengths. These spectra are consistent with nanophase hematite (e.g., Figure 6).

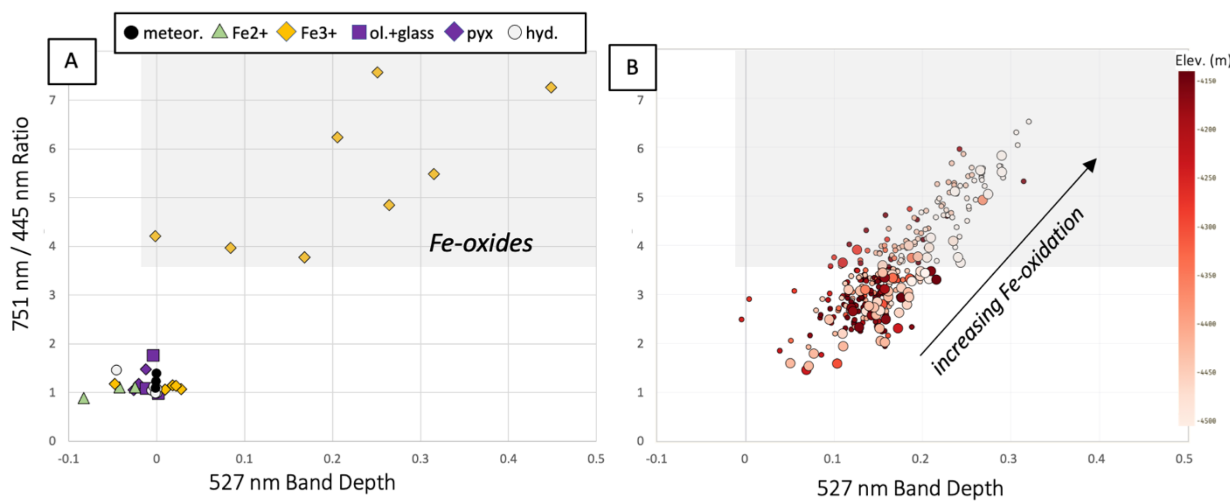

Figure 24. *Spectral parameters that distinguish Fe-oxides from other mineral phases are the 751 nm/445 nm ratio vs. 527 nm band depth, shown for: (a) Laboratory spectra of minerals convolved to Mastcam bandpasses: ferrous alteration phases (green triangles); pyroxenes (purple diamonds); olivines and basaltic glass (purple squares); ferric alteration phases (orange diamonds); iron meteorites (black circles), and hydrated minerals (white circles). Full spectra shown in Figures 6-7.. The gray shaded region in the upper right is only Fe-oxide minerals; (b) All Mastcam soil spectra, color coded by rover elevation, showing the interpretation of increasing Fe-oxide contributions in the upper right (changing grain sizes may also contribute).*

Table 7. *Summary of soil spectral classes.*

Class	Name	Short Description	Defining Spectral Characteristics	Type Examples	Distribution	Interpretation
1	**Yellowknife Bay**	Red, positive NIR slope	Large 751nm/445nm ratios; Large 527nm band depths; Large 1012nm/751nm ratios	Pearson, sol 66, mcam00478	Only seen near the landing site and in Yellowknife Bay	Strong influence of nanophase Fe-oxides and/or red hematite
2	**Bradbury**	Red, flat NIR profile	Large 751nm/445nm ratios; 1012nm/751nm ratio close to 1.0	Sparkle, sol 514, mcam02022	Prevalent throughout the Bradbury Group after leaving Yellowknife Bay	Spectra dominated by dust
3	**Goulburn**	Red, 908nm band	Large 751nm/445nm ratios; 1012nm/751nm ratios close to 1.0; Large 908nm band depth	Goulburn, sol 013, mcam00012	Only seen within scour marks at Bradbury Landing	Disturbance due to landing event
4	**Mt. Sharp**	Gray, flat to negative NIR slope	Small 751nm/445nm ratios; 1012nm/751nm ratio <1.0	Benbecula, sol 1964, mcam10270	Prevalent throughout the Mt. Sharp Group	Increasing contribution of mafic sand
5	**Bagnold**	Gray, strongly negative NIR slope	Peak reflectance at 751nm; Small 1012/751nm ratios; Positive 867nm band depths	Ogunquit, sol 1652, mcam08558	At and near the Bagnold Dunes	Olivine-bearing dark sands with very little dust

Class 3 (Goulburn) spectra are red and defined by prominent R4 (908 nm) band depths, and L6/L3 (1012 nm/751 nm) ratios close to 1.0, consistent with orthopyroxene spectra (e.g., Figure 6). Goulburn Class spectra only occur at the Bradbury Landing, within the scour marks where soil was disturbed by the retrorockets during the landing event, which generated significant local winds and mobilization of surface fines, extreme temperatures, and contamination by hydrazine exhaust. The unique soil spectra here may result from the landing event having cleared dust from the surface soils, potentially revealing the pyroxene signature of dust-free grains. This seems unlikely, however, given that we do not see the R4 (908 nm) band depth in any other low-dust, disturbed soils (e.g., wheel tracks) along the traverse. Alternative explanations are that the extreme heating resulted in highly localized mineralogic phase changes and/or differences in the IOF calibration for these earliest observations of the mission (which

were the only ones to use images of a near-dust-free calibration target). Throughout most of the traverse, Class 4 (Mt. Sharp) is the most prevalent class of soil spectra. These are less red than the Bradbury class, with flat to slightly negatively sloping NIR profiles (L6/L3 (1012 nm/751 nm) ratios ≤ 1.0). Class 5 (Bagnold) soil spectra are dark gray with low L6/L3 (1012 nm/751 nm) ratios and concave NIR profiles. This class includes soils within and near the Bagnold Dune Field, a collection of dark, active mafic sands.

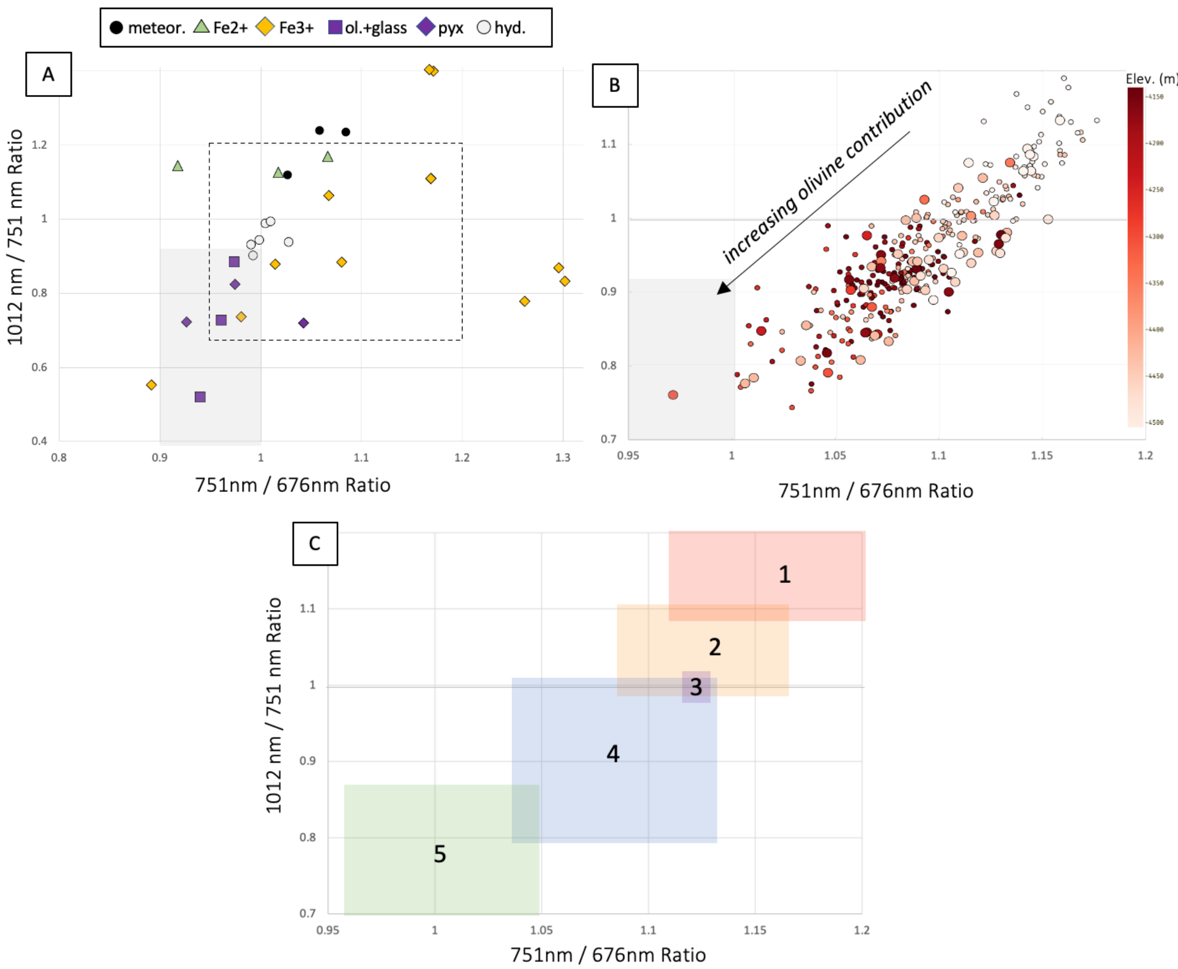

Figure 25. *The spectral parameters that best distinguish olivine from other mineral phases is the 1012 nm/751 nm ratio vs. 751 nm/676 nm ratio, shown for: (a) Laboratory spectra of minerals convolved to Mastcam bandpasses: ferrous alteration phases (green triangles); pyroxenes (purple diamonds); olivines and basaltic glass (purple squares); ferric alteration phases (orange diamonds); iron meteorites (black circles), and hydrated minerals (white circles). Full spectra shown in Figures 6-7.. The gray shaded region in the lower left is where olivine maps in this parameter space. The region bounded by the dashed line is that shown in b-c; (b) All soil spectra, color coded by rover elevation; (c) Soil spectral classes (Table 7).*

We have identified two parameter spaces that best distinguish the soil classes: (1) those that clearly separate Fe-oxide from other minerals (redness vs. L1 (527 nm) band depth; Figure 24) and (2) those that broadly separate olivines and pyroxenes from other minerals (L6/L3 (1012 nm/751 nm) ratio vs. L3/L4 (751 nm/676 nm) ratio; Figure 25). In both parameter spaces, the full dataset of soil spectra falls on a mixing line, with soils from early in the traverse towards the upper right (light-toned symbols) and soils from near the Bagnold Dunes in the lower left. Figure 25c shows the distribution of soil spectral classes in the "olivine" parameter space, ordered from 1-5 in the upper-right to lower-left. The only class that does not occupy a unique region in this space is the Goulburn Class, which overlaps with the Bradbury and Mt. Sharp Classes (which both have L6/L3 (1012 nm/751 nm) ratios close to zero). We interpret that the vast majority of the spectral diversity among soils in Gale crater, therefore, is due to the relative contributions of olivine-bearing sands vs. Fe-oxides from airfall dust and/or other sources.

We observe distinct trends in distributions of these soil classes with elevation across the traverse (Figure 26). At the lowest elevations, within the Yellowknife Bay formation, the soil spectra are dominated by the Yellowknife Bay and Bradbury Classes, which are the most red and most consistent with large contributions of Fe-oxides. Across the rest of Curiosity's traverse in the Bradbury Group, the Bradbury Class spectra are most prominent (with the exception of the landing site at -4501 m, which is the only location with Goulburn Class soils). The Mt. Sharp Class becomes increasingly more frequent after the contact with the Mt. Sharp Group strata and is the dominant soil spectral class at most higher elevations.

Near the two locations where Curiosity investigated the Bagnold Dune sands (a two-part campaign at elevations indicated in Figure 24), we observe the Bagnold Class spectra at targets within the Bagnold Dunes themselves, and at other dark soil deposits which likely have contributions of the dune sands. Seelos et al. (2014) identified variations in CRISM mafic mineral signatures at the Bagnold Dunes attributed to variable contributions of olivine and high-calcium pyroxene and showed that these spectral variations correlate with dune type and grain sorting (especially olivine enrichment on the upwind margin of the dune field). These observations were corroborated by Curiosity's observations of the dune field, where it found that the zones of stronger olivine signatures were qualitatively correlated with zones of inferred lower dust cover and higher rates of sand motion (Lapotre et al., 2017).

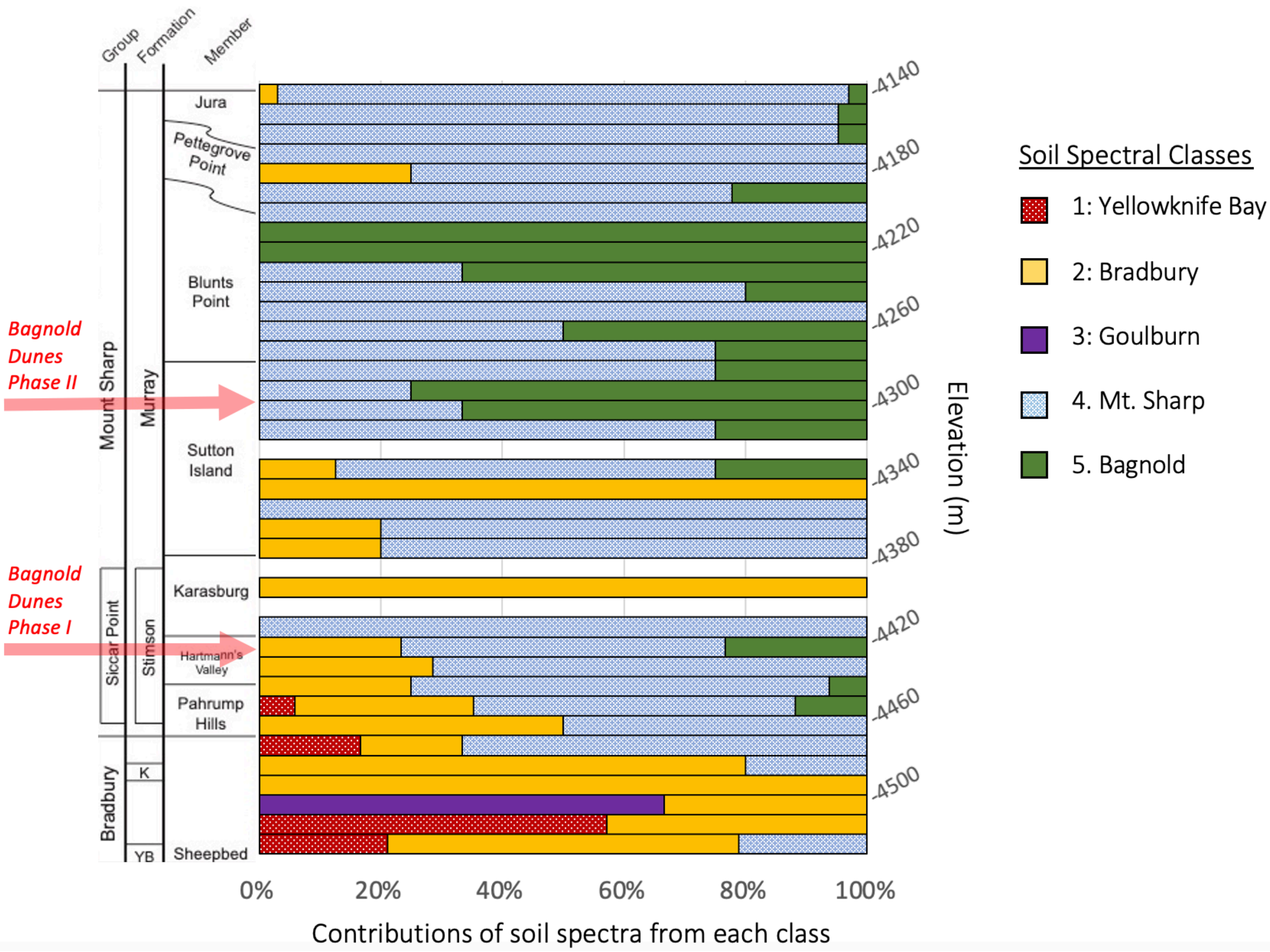

Figure 26. *Distribution of soil spectral classes with elevation across Curiosity's traverse. Data are binned to 10 m elevation intervals. Percentage values indicate proportions of the soil spectra belonging to each class within the elevation bin.*

The Bagnold Class is the only soil spectral class observed at the base of Vera Rubin ridge (immediately below the Pettegrove Point member), suggesting that the dark soils at this location are related to the Bagnold Dunes, and may be active aeolian deposits trapped against the base of the ridge. At a high level, these observations suggest that soils encountered early in the mission were largely inactive and spectrally dominated by dust and/or other Fe-oxides, whereas those later in the traverse are significantly less red and are spectrally dominated by contributions from the active, mafic dune fields.

4.1.3 Caveats

We acknowledge several limitations in our approach to define the spectral classes outlined above. Binning spectra into classes is a matter of judgement, and what we present here are not unique solutions for the dataset. There are degrees of variability lumped within each of our proposed classes, which could be reasonably split into subclasses. We also recognize that these classes are not exhaustive; there may be other spectral classes that are not included here because they were not included in our ROI selections (e.g., very small-scale features) or were only encountered once along the traverse.

Our database of end-member spectra is representative of the color diversity within each observation, but it also is not exhaustive. There may be spectrally distinct materials that have been overlooked because they do not appear distinct in the false-color and/or DCS composites used to identify the end-members. Our approach relies on a geologically trained human eye to identify the distinct color end members that are also geologically distinct, but judgement calls are often required, so we introduce biases associated with human error, training, and convention. An algorithm could perhaps be trained to identify such end-members, and similar attempts have been successful for novelty detection in Mastcam multispectral data (e.g., Kerner et al., 2020) and for identifying geologically-distinct materials in Navcam imagery (e.g. Francis et al., 2017). The training and implementation of such techniques is beyond the scope of this effort but will be explored in future work.

4.2 Implications for Erosion and Transportation of Sediments in Gale Crater

By comparing the spectral variations of soils and rocks across the traverse (Figure 15), and by examining the distributions of soil and rock spectral classes (Figures 22 and 26), we can test specific hypotheses about the origin of soils in Gale crater. If ongoing erosion of outcrops is contributing to the makeup of local soils, we would expect trends in spectral parameters for rocks and soils to parallel each other, which is not what we observe (Figure 18). If local mixing plays no part in soil composition, and if Gale crater soils are spectrally consistent with a "global Mars" soil and dust composition (e.g., Yen et al., 2005; Berger at al., 2016), we hypothesize that the soil spectral parameters would be near-uniform across the traverse, independent of rock spectral trends. We do not observe this pattern either, as soils do exhibit similar levels of spectral variability to the rocks, although with different trends (the exception being the L5 (867 nm) band depth, which has a much narrower spread of values than the rocks; Figure 18).

At the start of the traverse, where the Yellowknife and Bradbury Classes were encountered, the soil spectra were redder and had stronger L1 (527 nm) band depths than adjacent rock spectra, indicating increased levels of Fe-oxidation in soils relative to that observed on rock surfaces. These parameters likely correspond to large concentrations of dust in the soils near the beginning of Curiosity's traverse, consistent with CRISM data (Seelos et al., 2014) and dust cover indices from the Mars Global Surveyor (MGS) Thermal Emission Spectrometer

(TES) (Ruff & Christensen, 2002), in-situ observations of inactive soils near the landing site (e.g., Minitti et al., 2013), and APXS observations of dust thicknesses on rock surfaces generally decreasing along the traverse (Schmidt et al., 2018). The elevated Fe-oxidation parameters decrease with elevation (Figure 18; Figure 26), and Mt. Sharp Class soils are consistently less red than the rocks, with consistently negative NIR profiles (L6/L3 (1012 nm/751 nm) ratios <1.0), with Bagnold Class soils representing the end member of these spectral characteristics. No soils observed within the Mt. Sharp Group share spectral characteristics of the Marimba or Hexriver Class rocks in the region. Collectively, these observations imply that variable amounts of dark, mafic sands from the Bagnold Dunes – which are active in the modern aeolian environment – are the primary driver of spectral variability of soils throughout the Mt. Sharp Group. We find no evidence for a contribution of sediments derived from local bedrock.

Erosion of local rocks in the modern environment is certainly ongoing, however, as evidenced by the prevalence of active sands (e.g., Day & Kocurek, 2016; Baker et al., 2018), wind-sculpted textures (e.g., Bridges et al., 2014), cobble- and pebble-sized float clasts with spectra equivalent to adjacent outcrop (Figure 17). However, the Mastcam spectra show no indication of sand-sized or finer grains derived from local rocks that are mixing with nearby soils, at any point in the traverse. This is not unexpected, however, as the most spectral variability in the rocks of both groups occurs within the mudstones (grayer spectra due to a lack of oxidation in the Yellowknife Bay mudstones, redder spectra due to fine-grained hematite in the Murray mudstones), which erode into silt- to mud-sized grains that are more easily transported away by winds.

If local bedrock is eroding into cobble- and pebble-sized float clasts, which are being left as a surface lag, we hypothesize that float rocks can predict lithologies at higher elevations, as we might expect to encounter the same materials in outcrops further up in the section. We can test this hypothesis by comparing trends in float rock spectra to those of in-place outcrop in the multispectral database. We do not observe clear instances of float rock spectral parameters preceding the same parameters in overlying outcrop spectra; however, we observe the reverse phenomenon in the Sutton Island member. At elevations near -4330 m, outcrop spectra have 1012 nm / 751 nm ratios that are lower than had been observed previously in the mission, indicating negatively-sloped NIR profiles, and defined above as the Sutton Island Manset Class. In subsequent Mastcam observations, from elevations near -4310 m, a population of float rocks have this same NIR profile, although it is not seen in outcrop (Figure 17). This spectral class is associated with dark diagenetic features that are resistant to erosion (Haber et al., in prep), which may be the only parts of the overlying ~40 m of Sutton Island rocks in the section that remain as a cobble-sized lag of float rocks at this elevation.

5 Conclusions

We compiled a comprehensive database of Mastcam spectra for sols 0-2302 and quantified spectral variations across Curiosity's traverse in Gale crater through Vera Rubin ridge. As part of this effort, we adopted a number of conventions for analyzing Mastcam spectra, including: revised L0 and R0 Bayer blue band center wavelengths of 481 and 483, respectively; scaling the left- and right-cameras to their average value of the L6 (1012 nm) and R6 (1013 nm) filters; calculating spectral parameters exclusively from left- or right-camera filters; and opting to quantify spectral parameters as ratios instead of slopes.

In comparing dust-cleared surfaces (DRT targets and drill fines) to dusty rocks surfaces, we find that dust consistently masks rock spectra, resulting in higher reflectance (especially at longer wavelengths), muted VIS absorption features, and redder spectra (larger 751/445 nm ratios). However, the 867 nm band depth (which is consistent with fine-grained hematite) is more consistent between dusty and dust-cleared surfaces within the same rock units; therefore, the 867 nm band depth in dusty rock spectra reflects the actual spectral signature of the underlying rock. We find no evidence for atmospheric opacity (tau) influencing Mastcam spectra of surface rocks and soils, giving confidence that observed spectral trends across the traverse indicate real mineralogic variations

Based on PCA and an examination of spectral parameters across the entire traverse, we identified 9 rock spectral classes and 5 soil spectral classes. Rock classes are dominated by spectral differences attributed to hematite vs. other oxides, and are mostly confined to specific stratigraphic formations, except for the Dusty/Neutral Class (seen everywhere) and the Lebanon Class (iron meteorites punctuated across the traverse). Soil classes fall along a mixing line between spectra dominated by fine-grained Fe-oxides and those dominated by olivine-bearing sands. Like the rock classes, soil classes occur in specific sections of Curiosity’s traverse, with the reddest soils seen at the lowest elevations and darker, more mafic spectral signatures increasing with proximity to the Bagnold Dunes. The only soil spectral outlier class is the Goulburn Class, seen at Bradbury Landing, where the soils had been influenced by the landing event. Comparisons of rock and soil spectral trends have implications for the erosion of and transportation of sediments in Gale crater. The trends in soil spectra with elevation do not follow the trends observed in rock spectra, indicating that locally derived sediments are not significantly contributing to the spectra of soils. Rather, varying contributions of dark, mafic sands from the active Bagnold Dune field is the primary spectral characteristic of soils.

These spectral classes and their trends with stratigraphy through Vera Rubin ridge will provide a basis for comparison as Curiosity continues its ongoing ascent of Mt. Sharp. Based on orbital observations, which identified minerals such as Mg-sulfates, and opaline silica at higher elevations along the traverse (Milliken et al., 2008; Sheppard et al., 2020), we anticipate that Mastcam will encounter new spectral classes of rocks and/or soils as Curiosity explores these units. While detecting hydrated minerals with Mastcam is challenging, given the spacing of its longest-wavelength filters, our analyses of laboratory spectra suggest that Mastcam spectra can distinguish between mono-hydrated vs. poly-hydrated Mg-sulfate phases (e.g., kieserite vs. epsomite). Therefore, combined with chemical data from other Curiosity instruments, we expect that Mastcam spectra can play a key role interpreting mineralogy during the next stages of Curiosity's exploration.

Acknowledgements

We thank the Curiosity Science and Engineering Teams for their tremendous efforts over the many years of the mission, especially those responsible for planning, assessing, calibrating and archiving Mastcam data, including Malin Space Science Systems and their staff of Mastcam Payload Uplink Leads (PULs) and Payload Downlink Leads (PDLs) and the "calibration crew" at Arizona State University. We thank Alex Hayes and the Mars-2020 Mastcam-Z Team for sharing input from the radiometric calibration of Mastcam-Z and discussing implications for Mastcam. We also thank those who have contributed to the development of the Mastcam multispectral database while students at Western Washington University, including Acacia Arielle Evans, Natalie Moore, Amanda Rudolph, Sam Condon, Katelyn Frizzell, Kathleen Hoza, Jack Boyd, Baylee Adair and Abdullah Naimzadeh. MSR and AAF thank funding from the MSL Participating Scientist Program. Additionally, a portion of this research was carried out at the Jet

Propulsion Laboratory, California Institute of Technology, under a contract with the National Aeronautics and Space Administration (80NM0018D0004).

Open Research

All of the Mastcam multispectral image data used in this manuscript are freely available through the Planetary Data System Cartography and Imaging Sciences node (https://pds-imaging.jpl.nasa.gov/volumes/msl.html).

References

Adams, J. B. (1974), Visible and near-infrared diffuse reflectance spectra of pyroxenes as applied to remote sensing of solid objects in the solar system. *Journal of Geophysical Research, 79*, 4829–4836.

Baker, M. M., Lapotre, M. G. A., Minitti, M. E., Newman, C. E., Sullivan, R., Weitz, C. M., et al. (2018), The Bagnold Dunes in southern summer: Active sediment transport on Mars observed by the Curiosity rover. *Geophysical Research Letters, 45*, 8853– 8863. https://doi.org/10.1029/2018GL079040

Banham, S.G., Gupta, S., Rubin, D.M., Watkins, J.A., Sumner, D.Y., Edgett, K.S., et al. (2018), Ancient Martian aeolian processes and palaeomorphology reconstructed from the Stimson formation on the lower slope of Aeolis Mons, Gale crater, Mars. *Sedimentology, 65,* 993-1042. https://doi.org/10.1111/sed.12469.

Bell, J.F. III et al. (2000) Mineralogic and compositional properties of Martian soil and dust: Results from Mars Pathfinder. *Journal of Geophysical Research - Planets*, *105*, 1721–1755.

Bell, J.F., III, et al. (2003). Mars Exploration Rover Athena Panoramic Camera (Pancam) investigation, *Journal of Geophysical Research - Planets*, *108*, E12, 8063, https://doi.org/10.1029/2003JE002070.

Bell, J.F., III, Joseph, J., Sohl-Dickstein, J. N., Arneson, H. M., Johnson, M. J., Lemmon, M. T., & Savransky, D. (2006), In-flight calibration and performance of the Mars Exploration Rover Panoramic Camera (Pancam) instruments, *Journal of Geophysical Research – Planets*, *111*, E02S03, https://doi.org/10.1029/ 2005JE002444.

Bell, J.F., III, Godber, A., McNair, S., Caplinger, M. A., Maki, J. N., Lemmon, M. T. et al. (2017), The Mars Science Laboratory Curiosity rover Mastcam instruments: Preflight and in-flight calibration, validation, and data archiving, *Earth and Space Science, 4(7),* 396-452, https://doi.org/10.1002/2016EA000219.

Bell, J.F., III, Maki, J. N., Mehall, G. L., Revine, M. A., Caplinger, M. A., Bailey, Z. J. et al. (2020), The Mars 2020 Perseverance Rover Mast Camera Zoom (Mastcam-Z) Multispectral, Stereoscopic Imaging Investigation. *Space Science Reviews, 217(24).*

https://doi.org/10.1007/s11214-020-00755-x

Berger, J. A., Schmidt, M. E., Gellert, R., Campbell, J. L., King, P. L., Flemming, R. L., et al. (2016), A global Mars dust composition refined by the AlphaParticle X-ray Spectrometer in Gale Crater, *Geophysical Research Letters, 43*, 67–75, doi:10.1002/2015GL066675.

Bridges, N.T., Calef, F. J., Hallet, B., Herkenhoff, K. E., Lanza, N. L., Le Mouelic, S. (2014), The rock abrasion record at Gale Crater: Mars Science Laboratory results from Bradbury Landing to Rocknest, *Journal of Geophysical Research-Planets*, *119*, 1374-1389

Clark, R. N., & Roush, T. L. (1984). Reflectance spectroscopy: Quantitative analysis techniques for remote sensing applications. *Journal of Geophysical Research - Solid Earth, 89(B7),* 6329-6340. https://doi.org/10.1029/JB089iB07p06329.

Clark, R. N., King, T. V. V., Klejwa, M., Swayze, G. A., and Vergo, N. (1990), High spectral resolution reflectance spectroscopy of minerals, *Journal of Geophysical Research, 95(B8),* 12653– 12680, doi:10.1029/JB095iB08p12653.

Cloutis, E., M. Craig, L. Kaletzke, K. McCormack, and L. Stewart (2006a), HOSERLab: A new planetary spectrophotometer facility, Lunar Planet. Sci., XXXVII, Abstract 2121.

Cloutis, E. A., Hardersen, P. S., Bish, D .L., Bailey, D. T., Gaffey, M. J. & Craig, M. A. (2010), Reflectance spectra of iron meteorites: Implications for spectral identification of their parent bodies. *Meteoritics & Planetary Science, 45*, 304-332. https://doi.org/10.1111/j.1945-5100.2010.01033.x

Cousin, A., Sautter, V., Payré, V., Forni, O., Mangold, N., Gasnault, O. et al. (2017), Classification of igneous rocks analyzed by ChemCam at Gale crater, Mars, *Icarus, 288,* 265-283, https://doi.org/10.1016/j.icarus.2017.01.014.

Crowley, J. K. (1991), Visible and near-infrared (0.4–2.5 μm) reflectance spectra of Playa evaporite minerals, *Journal of Geophysical Research, 96(B10)*, 16231– 16240, doi:10.1029/91JB01714.

Czarnecki, S., Hardgrove, C., Gasda, P. J., Gabriel, T. S. J., Starr, M., Rice, M. S., et al. (2020), Identification and description of a silicic volcaniclastic layer in Gale crater, Mars, using active neutron interrogation. *Journal of Geophysical Research -Planets, 125*, e2019JE006180. https://doi.org/10.1029/2019JE006180.

Davis, J. C. (1973), Statistics and data analysis in geology, 3rd Edition. Wiley & Sons, Inc., New York.

Day, M., & Kocurek, G. (2016), Observations of an aeolian landscape: From surface to orbit in Gale Crater, *Icarus, 280*, 37-71, https://doi.org/10.1016/j.icarus.2015.09.042.

Edgar, L. A., Fedo, C. M., Gupta, S., Banham, S. G., Fraeman, A. A., Grotzinger, J. P., et al. (2020), A lacustrine paleoenvironment recorded at Vera Rubin ridge, Gale crater: Overview of the sedimentology and stratigraphy observed by the Mars Science Laboratory Curiosity rover. *Journal of Geophysical Research - Planets, 125*, e2019JE006307. https://doi.org/10.1029/2019JE006307.

Farrand, W.H., Bell, J.F. III, Johnson, J.R., Squyres, S.W., Soderblom, J., & Ming, D.W. (2006), Spectral variability among rocks in visible and near infrared multispectral Pancam data collected at Gusev Crater: Examinations using spectral mixture analysis and related techniques. *Journal of Geophysical Research-Planets, 111*, E02S15, https://doi.org/10.1029/2005JE002495.

Farrand, W.H., Bell, J.F. III, Johnson, J.R., Arvidson, R.E., Crumpler, L.S., Hurowitz, J.A., & Schröder, C. (2008), Rock spectral classes observed by the Spirit rover's Pancam on the Gusev crater plains and in the Columbia Hills. *Journal of Geophysical Research - Planets, 113*, E12S38, https://doi.org/10.1029/2008JE003237.

Farrand, W.H., Bell, J.F., Johnson, J.R., Rice, M.S., & Hurowitz, J.A. (2013), VNIR multispectral observations of rocks at Cape York, Endeavour crater, Mars by the Opportunity rover's Pancam. *Icarus, 225*, 709–725.

Fraeman, A. A., Ehlmann, B. L., Arvidson, R. E., Edwards, C. S., Grotzinger, J. P., Milliken, R. E., Quinn, D. P., & Rice, M. S. (2016), The stratigraphy and evolution of lower Mount Sharp from spectral, morphological, and thermophysical orbital data sets, *Journal of Geophysical Research - Planets, 121*, 1713– 1736, doi:10.1002/2016JE005095.

Fraeman, A. A., Edgar, L. A., Rampe, E. B., Thompson, L. M., Frydenvang, J., Fedo, C. M., et al. (2020a), Evidence for a diagenetic origin of Vera Rubin ridge, Gale crater, Mars: Summary and synthesis of Curiosity's exploration campaign. *Journal of Geophysical Research - Planets*, *125*, e2020JE006527. https://doi.org/10.1029/2020JE006527.

Fraeman, A. A., Johnson, J. R., Arvidson, R. E., Rice, M. S., Wellington, D. F., Morris, R. V., Fox, V. K., Horgan, B. H. N., Jacob, S. R., Salvatore, M. R., Sun, V. Z., Pinet, P., Bell, J. F. III, Wiens, R. C., & Vasavada, A. R. (2020b). Synergistic ground and orbital observations of iron oxides on Mt. Sharp and Vera Rubin ridge. *Journal of Geophysical Research - Planets*, *125*. https://doi.org/10.1029/2019JE006294

Francis, R., Estlin, T., Doran, G., Johnstone, S., Gaines, D., Verma, V. et al. (2017), AEGIS autonomous targeting for ChemCam on Mars Science Laboratory: Deployment and results of initial science team use. *Science Robotics, 2*(7), https://doi.org/10.1126/scirobotics.aan4582.

Frydenvang, J., Mangold, N., Wiens, R. C., Fraeman, A. A., Edgar, L. A., & Fedo, C. M., et al. (2020), The chemostratigraphy of the Murray Formation and role of diagenesis at Vera Rubin ridge in Gale Crater, Mars, as observed by the ChemCam instrument. *Journal of Geophysical Research - Planets, 125*, e2019JE006320. https://doi.org/10.1029/2019JE006320.

Grotzinger, J. P., Sumner, D. Y., Kah, L. C., Stack, K., Gupta, S., Edgar, L. et al. (2014), A habitable fluvio-lacustrine environment at Yellowknife Bay, Gale Crater, Mars, *Science, 343(6169)*, 1242777, https://doi.org/10.1126/science.1242777.

Guzewich, S. D., Lemmon, M., Smith, C. L., Martinez, G., Vicente-Retortillo, A., Newman, C. E., et al. (2019), Mars Science Laboratory observations of the 2018/Mars year 34 global dust storm. *Geophysical Research Letters, 46*, 71-79. DOI: 10.1029/2018GL080839.

Haber, J. T., Horgan, B., Fraeman, A. A., Johnson, J. R., Potter-McIntyre, S. L., Bell, J.F. III, et al. (2020), Diagenesis of an ancient lakeshore in Gale crater, Mars, from Mastcam multispectral images. *51st Lunar and Planetary Society Conference*, The Woodlands, TX.

Hapke, B. (1993) Theory of Reflectance and Emittance Spectroscopy, 469 p. Cambridge University Press.

Hayes, A.G., Corlies, P., Tate, C., Barrington, M., Bell, J. F. III, Maki, J. N. et al. Pre-Flight Calibration of the Mars 2020 Rover Mastcam Zoom (Mastcam-Z) Multispectral, Stereoscopic Imager. *Space Science Reviews, 217*, 29 (2021). https://doi.org/10.1007/s11214-021-00795-x

Jacob, S. R., Wellington, D. F., Bell, J. F., Achilles, C., Fraeman, A. A., Horgan, B., et al.

(2020), Spectral, compositional, and physical properties of the Upper Murray formation and Vera Rubin ridge, Gale crater, Mars. *Journal of Geophysical Research - Planets, 125*, e2019JE006290. https://doi.org/10.1029/2019JE006290.

Johnson, J. R., & Grundy, W. M. (2001), Visible/near-infrared spectra and two-layer modeling of palagonite-coated basalts, *Geophysical Research Letters, 28,* 2101 – 2104.

Johnson, J.R., Bell, J.F. III, Hayes, A., Deen, R., Godber, A., Joseph, et al. (2013), Preliminary Mastcam Visible/Near-Infrared Spectrophotometric Observations at the Curiosity Landing Site, Mars. *44th Lunar and Planetary Society Conference*, The Woodlands, TX.

Johnson, J.R., Meslin, P.-Y., Bell, J.F. III, Wiens, R., Maurice, S., Gasnalt, O., Rapin, W. (2020) Progress on iron meteorite detections by the Mars Science Laboratory Curiosity rover. Paper presented at *51st Lunar and Planetary Society Conference*, The Woodlands, TX.

Kerner, H. R., Wagstaff, K. L., Bue, B. D., Wellington, D. F., Jacob, S. Horton, P. et al. (2020), Comparison of novelty detection methods for multispectral images in rover-based planetary exploration missions. *Data Mining and Knowledge Discovery, 34*, 1642–1675. https://doi.org/10.1007/s10618-020-00697-6

Kinch, K. M., Bell, J.F . III, Goetz, W., Johnson, J. R., Joseph, J., Madsen, M. B., & Sohl-Dickstein, J. (2015), Dust deposition on the decks of the Mars Exploration Rovers: 10 years of dust dynamics on the Panoramic Camera calibration targets. *Earth and Space Science, 2*, 144–172.

Kokaly, R. F., Clark, R. N., Swayze, G. A., Livo, K. E., Hoefen, T. M., Pearson, N. C., et al. (2017), USGS Spectral Library Version 7: U.S. Geological Survey Data Series 1035, 61 p., https://doi.org/10.3133/ds1035.

Lanza, N.L., Wiens, R. C., Arvidson, R. E., Clark, B. C., Fischer, W. W., Gellert, R. et al. (2016), Oxidation of manganese in an ancient aquifer, Kimberley formation, Gale crater, Mars, *Geophysical Research Letters, 43(14*), 7398-7407, https://doi.org/10.1002/2016GL069109.

Lapotre, M. G. A., Ehlmann, B. L., Minson, S. E., Arvidson, R. E., Ayoub, F., Fraeman, A. A., Ewing, R. C., & Bridges, N. T. (2017), Compositional variations in sands of the Bagnold Dunes, Gale crater, Mars, from visible-shortwave infrared spectroscopy and comparison with ground truth from the Curiosity rover, *Journal of Geophysical Research - Planets, 122*, 2489– 2509, doi:10.1002/2016JE005133.

Lemmon, M. T., Guzewich, S. D., McConnochie, T., de Vicente-Retortillo, A., Martinez, G., Smith, M. D. et al. (2019), Large dust aerosol sizes seen during the 2018 Martian global dust event by the Curiosity rover. *Geophysical Research Letters, 46*, 9448-9456. https://doi.org/10.1029/2019GL084407.

Malin, M. C., Ravine, M. A., Caplinger, M. A., Ghaemi, F. T., Schaffner, J. A., Maki, J. N. et al. (2017), The Mars Science Laboratory (MSL) Mast cameras and Descent imager: Investigation and instrument descriptions, *Earth and Space Science, 4(8),* 506-539, https://doi.org/10.1002/2016EA000252.

Mangold, N., Schmidt, M. E., Fisk, M. R., Forni, O., McLennan, S. M., Ming, D. W. et al. (2017), Classification scheme for sedimentary and igneous rocks in Gale crater, Mars, *Icarus, 284*, 1-17, https://doi.org/10.1016/j.icarus.2016.11.005.

Minitti M.E., Kennedy M.R., Krezoski G.M., Rowland S.K., Schieber J. et al. (2017), Using MARDI Twilight Images to Assess Variations in the Murray Formation with Elevation, Gale

Crater, Mars. *48^{th} Lunar and Planetary Society Conference*, The Woodlands, TX.

Morris, R. V., Lauer, H. V., Jr., Lawson, C. A., Gibson, E. K., Jr., Nace, G. A. & Stewart, C. (1985), Spectral and other physicochemical properties of submicron powders of hematite (a-Fe2O3), maghemite (g-Fe2O3), magnetite (Fe3O4), goethite (a-FeOOH), and lepidocrocite (g-FeOOH), *Journal of Geophysical Research, 90*, 3126–3144, https://doi.org/10.1029/JB090iB04p03126.

Nachon, M., Clegg, S. M., Mangold, N., Schröder, S., Kah, L. C., Dromart, G. et al. (2014), Calcium sulfate veins characterized by ChemCam/Curiosity at Gale Crater, Mars, *Journal of Geophysical Research Planets, 119(9)*, 1991-2016, doi:10.1002/2013JE004588.

Pedgregosa, F., Varoquax, G., Gramfort, A., Michel, V., Thirion, B., et al. (2011), Scikit-learn: Machine Learning in Python, *Journal of Machine Learning Reserch, 12*, 2825-2830. https://doi.org/10.5555/1953048.2078195.

Rampe, E. B., Bristow, T. F., Morris, R. V., Morrison, S. M., Achilles, C. N., Ming, D. W., et al. (2020), Mineralogy of Vera Rubin ridge from the Mars Science Laboratory CheMin instrument. *Journal of Geophysical Research - Planets, 125*, e2019JE006306. https://doi.org/10.1029/2019JE006306

Rapin, W., Meslin, P.-Y., Maurice, S., Vaniman, D., Nachon, M., Mangold, N. et al. (2016), Hydration state of calcium sulfates in Gale crater, Mars: Identification of bassanite veins, *Earth and Planetary Science Letters, 452*, 197-205, doi:10.1016/j.epsl.2016.07.045.

Reid, R.J., Smith, P. H., Lemmon, M., Tanner, R., Burkland, M., Wegryn, E. et al. (1999). Imager for Mars Pathfinder (IMP) image calibration, *Journal of Geophysical Research - Planets, 104*, 8907–8926, https://doi.org/10.1029/1998JE900011.

Rice, M.S., Bell, J.F., III, Cloutis, E., Wang, A., Ruff, S., Craig, M. A. et al. (2010). Silica-rich deposits and hydrated minerals at Gusev crater, Mars: Vis-NIR spectral characterization and regional mapping, *Icarus, 205*, 375–395, https://doi.org/10.1016/j.icarus.2009.03.035.

Rice, M.S., Bell, J.F., III, Cloutis, E., Wray, J. J., Herkenhoff, K. E., Sullivan, R., Johnson, J. R. & Anderson, R. B. (2011). Temporal observations of bright soil exposures at Gusev crater, Mars, *Journal of Geophysical Research - Planets, 116*, E00F14, https://doi.org/10.1029/2010JE003683.

Rice, M. S., Cloutis, E., Bell, J.F., III, Mertzman, S. A., Bish, D. L., Craig, M., Mountain, B., Renaut, R. W. and Gautason, B. (2013), Reflectance spectra diversity of silica-rich materials: Sensitivity to environment and implications for detections on Mars, *Icarus, 223*, 499–533, https://doi.org/10.1016/j.icarus.2012.09.021.

Rice, M. S., Gupta, S.,Treiman, A. H., Stack, K. M., Calef, F., Edgar, L. A., et al. (2017). Geologic overview of the Mars Science Laboratory rover mission at The Kimberley, Gale crater, Mars, *Journal of Geophysical Research - Planets, 122(1),* 2-20, https://doi.org/10.1002/2016JE005200.

Rice, M. S., Reynolds, M., Studer-Ellis, G., Bell, J. F., III, Johnson, J. R., Herkenhoff, K. E., et al. (2018). The albedo of Mars: Six Mars years of observations from Pancam on the Mars Exploration Rovers and comparisons to MOC, CTX and HiRISE. *Icarus, 314*, 159–174. https://doi.org/10.1016/j.icarus.2018.05.017

Ruff, S. W., & Christensen, P. R. (2002), Bright and dark regions on Mars: Particle size and mineralogical characteristics based on Thermal Emission Spectrometer data, *Journal of*

Geophysical Research - Planets., *107(E12),* 5127, doi:10.1029/2001JE001580.

Ruff, S. W., Farmer, J. D., Calvin, W. M., Herkenhoff, K. E., Johnson, J. R., Morris, R. V. et al. (2011), Characteristics, distribution, origin, and significance of opaline silica observed by the Spirit rover in Gusev crater, Mars, *Journal of Geophysical Research - Planets*, *116*, E00F23, https://doi.org/10.1029/2010JE003767.

Schmidt, M. E., Perrett, G. M., Bray, S. L., Bradley, N. J., Lee, R. E., Berger, J. A., et al. (2018), Dusty rocks in Gale crater: Assessing areal coverage and separating dust and rock contributions in APXS analyses. *Journal of Geophysical Research - Planets, 123*, 1649–1673. https://doi.org/10.1029/2018JE005553

Singer, R. B. (1982), Spectral evidence for the mineralogy of high-albedo soils and dust on Mars. *Journal of Geophysical Research - Solid Earth*, 87, 10159–10168.

Smith, P. H., Tomasko, M. R., Britt, D., Crowe, D. G., Reid, R., Keller, H. U., et al. (1997). The imager for Mars Pathfinder experiment, *Journal of Geophysical Research – Planets, 102*, E2, 4003-402. https://doi.org/10.1029/96JE03568.

Smith, P. H., Tamparri, L., Arvidson, R. E., Bass, D., Blaney, D., Boynton, W., et al. (2008). Introduction to special section on the Phoenix Mission: Landing Site Characterization Experiments, Mission Overviews, and Expected Science, *Journal of Geophysical Research – Planets, 113*, E12, https://doi.org/10.1029/2008JE00308.

Thompson, L. M., Berger, J. A., Spray, J. G., Fraeman, A. A., McCraig, M. A., O'Connell-Cooper, C. D., et al. (2020), APXS-derived compositional characteristics of Vera Rubin ridge and Murray formation, Gale crater, Mars: Geochemical implications for the origin of the ridge. *Journal of Geophysical Research - Planets, 125*, e2019JE006319. https://doi.org/10.1029/2019JE006319

Vasavada, A. R., Grotzinger, J. P., Arvidson, R. E., Calef, F. J., Crisp, J. A., Gupta, S. et al. (2014), Overview of the Mars Science Laboratory mission: Bradbury landing to Yellowknife Bay and beyond, *Journal of Geophysical Research - Planets, 119(6),* 1134-1161, https://doi.org/10.1002/2014JE004622.

Wellington, D. F., Bell, J. F., III, Johnson, J. R., Kinch, K. M., Rice, M. S., Godber, A. et al. (2017), Visible to Near-Infrared MSL/Mastcam Multispectral Imaging: Initial Results from Select High-Interest Science Targets within Gale Crater, Mars, *American Mineralogist,* https://doi.org/10.2138/am-2017-5760CCBY.

Wellington, D. F., Johnson, J. R., Meslin, P. Y., & Bell, J. F., III (2018), Iron Meteorite Candidates Within Gale Crater, Mars, from MSL/Mastcam Multispectral Observations. *49^{th} Lunar and Planetary Society Conference*, The Woodlands, TX.

Wellington, D. F., Meslin, P. Y., Van Beek, J., Johnson, J. R., Wiens, R. C., Calef, F. J., & Bell, J. F. (2019), Iron Meteorite Finds Across Lower Mt. Sharp, Gale Crater, Mars: Clustering and Implications. *50^{th} Lunar and Planetary Society Conference*, The Woodlands, TX.

Rapin, W. Meslin, P.-Y. Maurice, S,. Vaniman, D., Nachon, M., Mangold, N. et al. (2016), Hydration state of calcium sulfates in Gale crater, Mars: Identification of bassanite veins, *Earth and Planetary Science Letters, 452*, 197-205, https://doi.org/10.1016/j.epsl.2016.07.045.

Yen, A. S., Gellert, R., Shroder, C., Morris, R. V., Bell, J. F., III, Knudson, A. T., et al. (2005), An integrated view of the chemistry and mineralogy of Martian soils, *Nature, 436(7047),* 49–54, https://doi.org/0.1038/nature03637.